Benjamin Lageder, BSc

Functionalization of the surface of titanium by addition of magnesium

MASTER'S THESIS

to achieve the university degree of

Diplom-Ingenieur

Master's degree programme: Advanced Materials Science

submitted to

Graz University of Technology

Supervisor

Univ.Prof. Dipl.-Ing. Dr.techn. Christof Sommitsch
Co-Supervisor: Dr.techn. Fernando Gustavo Warchomicka

Institute of Materials Science, Joining and Forming
Head: Univ.Prof. Dipl.-Ing. Dr.techn. Christof Sommitsch

Graz, June 2017

AFFIDAVIT

I declare that I have authored this thesis independently, that I have not used other than the declared sources/resources, and that I have explicitly indicated all material which has been quoted either literally or by content from the sources used. The text document uploaded to TUGRAZonline is identical to the present master's thesis.

_____

Date

_____

Signature

Acknowledgement

There are a lot of people who contributed in one way or another to the completion of this thesis, to whom I would like to express my gratitude.

First of all, I would like to thank the Institute of Materials Science, Joining and Forming (IMAT) and especially *Univ.Prof. Dipl.-Ing. Dr.techn. Christof Sommitsch* to have given me the opportunity to do my master's thesis at this institute.

Thanks are due to the secretary and the laboratory team, who would help me with organizational and practical work respectively, as well as other members of the institute for sharing their knowledge and technical know-how and who would often give me suggestions and advice.

Most importantly, I would like to thank my supervisor, *Dr.techn Fernando Warchomicka*, whose guidance and supervision were essential during this work and who was always ready to discuss and help me with any of my questions.

I would particularly like to thank my parents, who supported me throughout all my studies and without whose help I would not be able to be where I am at the moment, as well as my friends who made Graz a second home for me.

Abstract

Both magnesium and titanium and their respective alloys have been investigated extensively with respect to their applicability as biomaterials. While titanium is known for its outstanding corrosion resistance and biocompatibility but inert behaviour, magnesium is a bioactive material which degrades gradually over time in body environment and thus prevents the necessity of a second invasive surgery. The functionalization of titanium surface by addition of magnesium is the aim of this work. The challenge in joining these two metals is their lack of mutual solubility or formation of intermetallic phases.

In the present work electron beam welding is used to create a bond between titanium Grade 2 and pure magnesium or a magnesium alloy Mg2Ag. A two-dimensional joining is obtained by deflecting the electron beam according to a beam figure designed in MATLAB.

By an optimization of the design of the beam figure and welding parameters, welding defects can be minimized and a good bonding between the two metals can be reached. Surface finish examination suggest good finish and suitable roughness for both magnesium and titanium and an increased titanium hardness due to martensite formation.

The Mg2Ag alloy exhibits a finer microstructure with a dendritic structure with local segregation of silver and a formation of precipitates upon ageing. In addition to antibacterial properties, silver provides the opportunity to tailor mechanical properties and corrosion behaviour of the magnesium-based layer.

The favourable characteristics of the used materials and the assembly as well as the through the process induced surface modifications and microstructures are hoped to lead to improvements in implant-tissue interaction and to be applied in future biomedical applications.

Kurzfassung

Die Untersuchung von Titan und Magnesium sowie deren Legierungen für den Einsatz als Biomaterialien ist Gegenstand aktueller Forschung. Titan besitzt exzellente Korrosionsbeständigkeit sowie Biokompatibilität, weist jedoch ein inertes Verhalten auf. Magnesium hingegen ist ein bioaktives Material, welches im Körper mit der Zeit degradiert und dadurch die Notwendigkeit einer zusätzlichen Operation zur Entfernung des Implantates vermeiden lässt. Die Funktionalisierung der Titanoberfläche durch Aufbringen einer bioaktiven Schicht aus Magnesium ist das Ziel dieser Arbeit. Eine Herausforderung stellt dabei die sehr geringe gegenseitige Löslichkeit der beiden Metalle sowie das Fehlen intermetallischer Phasen dar.

In dieser Arbeit wird mittels Elektronstrahl eine Verbindung zwischen Titan Grade 2 und purem Magnesium sowie einer Magnesium-Silber Legierung (Mg2Ag) geschaffen. Die Strahlablenkung zur Erzeugung einer flächigen Verbindung wird über eine mit MATLAB erstellte Ablenkfigur gesteuert.

Durch stetige Optimierung des Designs der Ablenkfiguren und der Schweißparameter können Schweißdefekte verringert und eine gute Verbindung zwischen Magnesium und Titan erzeugt werden. Die Untersuchung der Oberfläche zeigt gute Beschaffenheit und geeignete Rauheit sowohl für Magnesium als auch für Titan. Des Weiteren kann die Härte der Titanoberfläche durch Bildung von Titanmartensit erhöht werden.

Durch den Elektronenstrahl wird in der Mg2Ag-Legierung eine feine Mikrostruktur erzeugt, wobei es zu einer lokalen Segregation von Silber kommt. Durch Wärmebehandlung können in Folge intermetallische Ausscheidungen an den Korngrenzen erzeugt werden. Zusätzlich zu den antibakteriellen Eigenschaften ermöglicht das Legieren mit Silber somit eine Veränderung der mechanischen sowie der Korrosionseigenschaften der Magnesiumschicht.

Die vorteilhaften Eigenschaften der verwendeten Materialien und die Verbindung derselben sowie die durch den Schweißprozess bewirkten Oberflächenveränderungen und Mikrostrukturmodifikationen sollten zur Verbesserung der Interaktion zwischen Implantat und Körper führen und einen zukünftigen Einsatz als Biomaterial ermöglichen.

Contents

1 Introduction

Both magnesium and titanium are key materials for medical applications due to their physical, mechanical, chemical and biological properties. Both are employed already in medicine in various fields of application. Many studies have been conducted regarding their potential in transplant technology and both their strengths and constraints have been determined. Improvements of their properties by alloying bulk material or by various surface modification techniques are being conducted to design biomedical materials suitable for several applications. The field of medical implants is wide as for different implant locations and replacement of distinct tissues a diverse range of requirements needs to be met.

The present work investigates the functionalization of titanium surface by creation of a two-component system with magnesium, joint by electron beam welding (EBW). Titanium Grade 2 is used as a base material and pure magnesium as well as a Mg-2 wt.%Ag alloy as a surface coating layer. Process parameters are determined and optimized after examination of the outcome considering various characteristics such as quality of the joint, porosity and surface finish.

In the first part the current state of the art is disclosed by presenting the range of biomaterials in use today and further elaborating current developments in the field of titanium- and magnesium-based implants, exposing their respective benefits and drawbacks. Furthermore, the challenge for an assembly of titanium and magnesium are highlighted and electron beam welding as a possible technique to solve this problem presented.

In chapter three, the execution of experiments is explained covering preparation, manufacturing (including used parameters) and characterization of the samples.

In chapter four, the results are given and the influence of the parameters are addressed. Furthermore, the obtained results are linked to the consequences for potential application as biomaterials.

Finally, the results are summarised, a short conclusion is drawn and an outlook for further investigations in this field is given.

2 State of the art

2.1 Biomaterials

Biomaterials are a class of materials suitable for introduction into living tissue and are used to replace a part or a function of the body [1]. Biomaterials need to feature certain properties in order to be employed successfully in a living tissue. These properties need to ensure compatibility by not being toxic, injurious, carcinogenic, physiologically reactive and not causing immunological rejection, and are often summarised by the term biocompatibility [2]. Biocompatibility is defined as the "ability of a material to perform with an appropriate host response in a specific situation" [3].

Biomaterials need to provide a certain function in the body (like replacement of a bone). For that matter, the interface reaction between implant and body tissue is of fundamental importance. Material and biological tissue can be modified by each other as interaction between the two occurs. The reaction of the tissue to the introduction of the biomaterial can be classified into three categories [2]:

- biotolerant materials: separated from the bone tissue by a layer of fibrous tissue

- bioinert materials: in direct contact with the tissue, but no chemical reaction occurs

- bioactive materials: establish chemical bonds with the bone tissue (e.g. osseointegration)

Some other important definitions concerning bone healing are [4]:

- Osseointegration: direct contact between living bone and implant (anchorage of an implant by the formation of bony tissue around the implant)

- Osteoconduction: permits bone growth on its surface or down into pores or channels, thereby increasing interfacial area (morphological fixation)

- Osteoinduction: stimulation of bone formation (osteogenesis)

Although biomaterials have been around since ancient times (with dental implants being one of the earliest biomaterials), serious research concerning biomaterials is a recent development going back only a few decades. As no one materials is suitable for all biomaterial application, the study of biomaterials is a field of continuous research [1].

The object of early biomaterials was to find materials with suitable physical and mechanical properties for the respective application. This included them being bioinert, i.e. having no or very little interaction with the tissue. The lack of a chemical or biological bond can result in relative movement at the biomaterial-tissue interface and eventually lead to deterioration of one or both components. The second generation of biomaterials moved to bioactive materials which have controlled reactions with the tissue to induce a therapeutic effect. Also resorbable materials are part of this class. The third generation focuses on the development of biomaterials supporting and stimulating the regeneration of functional tissue (biointeractive) [5].

Furthermore, the success of a biomaterial depends on the specific implant location and the condition of the patient. Dependent on those factors the requirements for a biomaterial may change: Properties like fatigue and wear need to be considered and the biomaterial chosen and adapted accordingly (for example by surface modifications) [1].

Biomaterial science is a multidisciplinary field and many classes of materials are being used as biomaterials: ceramics and glasses, polymers, metals and composites.

Ceramic biomaterials: Ceramics are generally biocompatible and can be designed as bioinert or resorbable as required. Ceramic biomaterials are often used in dental replacements. Examples for bioceramics are alumina, zirconia and calcium phosphates. However, their brittle behaviour and their low strength in tension limit their application [1, 5].

Polymeric biomaterials: Polymers are easy to fabricate and resilient. Because of their great variety and modifiable properties polymers are widely used in implant technology. General disadvantages of polymer biomaterials are their susceptibility to degradation and deformation with time and their lower strength in comparison to metals and ceramics [1, 5].

Metallic biomaterials: Metals are used for their favourable mechanical properties, but are susceptible to corrosion which can weaken the implant and release harmful corrosion products. Metals are quite easy to process and have good finish qualities. Commonly used metals as biomaterials are stainless steels, CoCr alloys and titanium alloys. Alloying, processing and heat treatments allow to modify the properties of these metals.

Stainless steels like 316L have a long history in implant technology. The great advantage of stainless steels is their wide range of mechanical properties depending on chemical composition and processing history. The properties can therefore be tailored to each specific application. However, the corrosion resistance in the human body is reduced compared to CoCr- and titanium alloys, with inclusions representing possible corrosion initiation sites [5].

Cobalt-chromium alloys are used in dentistry and for heavy loaded joints. Chromium enhances the corrosion resistance and strengthens the alloy by solid solution. The alloy has high hardness and toughness and has superior fatigue and ultimate strength properties suitable for applications requiring long service life. However, the high modulus of elasticity may result in stress shielding and particulate cobalt release induce toxicity in the tissue [6].

2.1.1 Biodegradable materials

Degradability is desirable whenever an implant only serves a temporary purpose. This may be the case for children with growing bone structures and for all temporary implants to avoid a second invasive surgery for implant removal. The majority of biodegradable materials in use today are polymers. However, for hard tissue repair corrodible metals (e.g. magnesium) proved to be a promising alternative [7]. Biodegradable metals are designed to provide temporary mechanical support and to eventually dissolve in vivo when they are no longer needed [7]. Therefore, biodegradation rates and modes need to be controlled to match the healing rates of the host tissues in order to preserve mechanical integrity until recovery. This can be accomplished through alloying and coating in order to improve mechanical properties and attain more predictable degradation behaviour [7].

Furthermore, an appropriate host response elicited by released corrosion products is essential: The corrosion products need to be biocompatible and be able

4

to be metabolized by the human body [8]. Moreover, bioactive biomaterials are being developed towards third-generation biomedical materials by exploiting the continuous chemical production of biodegradation products to assist local tissue reconstruction (osseoinduction) [7].

2.2 Titanium

Titanium is an allotropic material: hexagonal closed packed structure (HCP, α-Ti) at low temperature up to 882.5℃ and body-centerd cubic (BCC, β-Ti) above [6]. Depending on the alloying elements either the α-Ti phase or the β-Ti phase is stabilized at room temperature modifying elastic modulus and strength of the material [5].

Titanium has been used in medical application for more than 50 years due to its favourable mechanical, chemical and physical properties [9]. Titanium is characterised by high strength, low weight and outstanding corrosion resistance.

Commercial pure titanium has an elastic modulus of 100-110 GPa, much lower than other metal alloys, but yet significantly higher than natural bone (3-20 GPa) which may still cause stress shielding, bone resorption and implant loosening, and contribute to early failure of the implant [10]. Also, the density of titanium (4.2 g/cm^3) [9], although smaller when compared to steel and other metals used in biomedical applications, is significantly higher than that of natural bone (1.8-2.1 g/cm^3) [11]. Because of its low density the specific strength is much higher compared to other implant materials. By alloying titanium the strength can be further increased while reducing its ductility.

The applicability of titanium as an implant material, however, is not just determined by the bulk properties, but also by the surface characteristics which play an important role to avoid implant failure or rejection [9]. A good bonding between the surface of the implant and the surrounding tissue is essential for load transmission between bone and implant [12].

By forming a stable, repassivating, chemically inert, continuous and corrosion-resistant oxide layer (in general TiO_2), titanium surfaces show passive properties [5, 6, 13]. Titanium is also relatively bioinert to all body fluids and proved good

biocompatibility and no allergenic response [5, 10]. In addition, titanium showed the capability of osseointegration by forming a direct interface with bone and being able to join also with other tissue and qualifies therefore for long-lasting implants [5].

However, because of its low hardness, titanium exhibits a low wear and abrasion resistance, which can result in a reduced service life of the implant and a release of Ti and TiO_2 particles [6, 9]. Although titanium proved excellent biocompatibility as a bulk metal [12], this is not true for released ions. For titanium, the safe ion concentration, up to which no influence on cell proliferation and viability was found, was determined to 15.5 µg/L [10]. The toxic effect resulting from release of other alloying elements needs to be considered as it influences the biocompatibility and can cause problems eventually leading to implant failure [12].

2.2.1 Functionalization of Titanium

The implant surface can be modified by biological, chemical or physical methods. Surface treatments are performed to improve osseointegration, bioactivity, biocompatibility and corrosion or wear resistance [5]. Moreover, surface modifications towards antibacterial surfaces can prevent implant failure by bacterial infection [9].

Topographical modifications on titanium proved to boost the success rate of implant therapy and to significantly reduce the healing period [14]. Increased surface roughness of the implant increased cellular attachment and osteoblast activity and ensured a better implant surface-bone contact and increased mechanical retention [15].

The quality of the oxide surface layer is fundamental for corrosion resistance and wear resistance likewise. Nitriding techniques (e.g. diffusion, ion implantation) are frequently used to synthesize surface layers rich in TiN and TiN_2 in order to increase passitivity and improve wear resistance [16, 17]. Laser irradiated and dual-acid etched surfaces showed an improved bone damage repair and suggested enhanced osteoconductivity compared to non-treated titanium [18]. Moreover, corrosion resistance was found to be improved significantly after laser treatment [19]. A lot of research has been conducted in producing nanorough surfaces on titanium. Richard et.al. showed that nano-titania and zirconia coatings on titanium

substrates exhibited high wear resistance and corrosion resistance while biocompatibility was preserved [20].

Research is also being conducted into biological functionalization of implant coatings (e.g. biomimetic calcium phosphate coatings) to promote local bone formation, direct material-bone bonding or the activation of particular cell responses by the use of specific biomolecules [5, 21].

Other surface modification methods to potentially improve electrochemical characteristics and hence the life span of titanium are manifold: physical and chemical vapour deposition, laser cladding, thermal and plasma spraying, thermal oxidation, sandblasting, electrochemical treatment, machining [22].

2.3 Magnesium

Magnesium is used as a biomaterial because of its advantageous mechanical properties and biodegradability [23], degrading in vivo and hence, eliminating the need of a second invasive surgery to remove the implant [24]. Magnesium has properties similar to natural bone with a density of 1.74 g/cm^3 and a Young's modulus of 41-45 GPa compared to 1.8-2.1 g/cm^3 and 3-20 GPa of natural bone. This minimizes stress shielding and the resulting reduced stimulation of new bone growth [11].

Moreover, magnesium shows good biocompatibility without systemic inflammatory reaction or affecting the cellular blood composition [25, 26]. Magnesium is also naturally present in the human body and bone tissue and essential to human metabolism [11]. Furthermore, the complete degradation of the magnesium suggests the corrosion products are either phagocytosed or dissolved and eliminated via the kidneys [24].

In aqueous environments an electrochemical reaction with water takes place with the production of magnesium hydroxide and hydrogen gas [27] (see figure 1). Mg dissolves as Mg^{2+} which reacts with water, generates hydrogen bubbles and creates hydroxyl groups. Dissolved Mg^{2+} ions react with hydroxyl groups and precipitate as magnesium hydroxide forming a passive interlayer on the degradation surface together with magnesium oxide [8].

$$2\,H_2O + 2\,e^- \longrightarrow H_2 + 2\,OH^- \qquad \text{(cathodic partial reaction)}$$

$$Mg \longrightarrow Mg^{2+} + 2\,e^- \qquad \text{(anodic partial reaction)}$$

$$Mg^{2+} + 2\,OH^- \longrightarrow Mg(OH)_2 \qquad \text{(product formation)}$$

$$Mg + 2\,H_2O \longrightarrow Mg(OH)_2 + H_2 \quad \text{(overall reaction)}$$
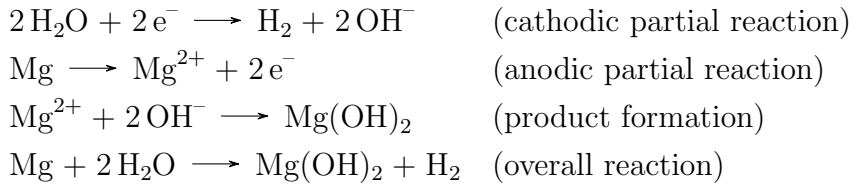
The formation of the hydroxide protective film decreases the corrosion rate but is not as stable as on other metals and prone to pitting, especially in immersed conditions and in the presence of chloride ions [11, 28, 35]. The pitting corrosion changes the surface topology and was found to create network-like cracks and small pits [24, 28]. Also, hydrogen embrittlement occurs along grain boundaries and magnesium particles are physically detached by hydrogen stress cracking (chunk effect) [8]. However, during corrosion released OH⁻-ions lead to a pH-increase [28] which in turn reduces the corrosion rate [27] (passivation zone in the Pourbaix diagram in figure 1).
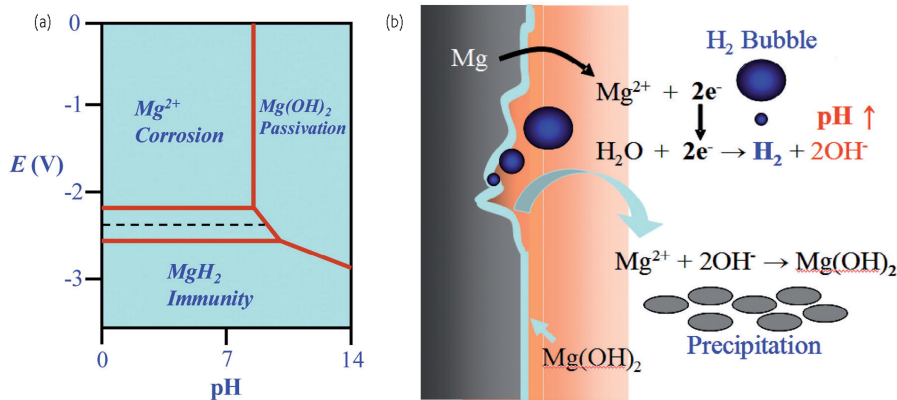
Figure 1: Pourbaix diagramm and corrosion mechanism in water of magnesium [8]

Too fast degradation also leads to the formation of large hydrogen gas volume [24]. For each atom of magnesium, one molecule of hydrogen gas is formed. However, little adverse effects due to the gas bubbles were observed [24], inducing some mechanical disturbance of bone regeneration and resulting in callus formation, but ultimately recovering to the status quo after complete degradation. Smaller degradation rates produced less gas evolution with the tissue being able to carry off the hydrogen [27].

For degradable magnesium implants the bone mass surrounding the magnesium

was found to be enhanced compared to polymer implants [24]. During implant degradation, the surface of the magnesium is coated with a newly formed mineral phase consisting mainly of calcium phosphate [24]. This conversion layer is in direct contact with the surrounding bone proving the good osteoconductive properties of the released magnesium ions by enhancing the formation of new bone tissue directly at the surface [27, 29]. The increased activity of the osteoblasts might be explained by the important role magnesium ions play in the structural biology of nucleic acids [24].

Bone-implant interface strength and osseointegration were demonstrated to be significantly greater for magnesium than for conventional titanium materials [26]. Also, the increased surface roughness due to surface corrosion enhances the mechanical attachment between implant and bone [26]. Magnesium was further shown to have a higher antibacterial activity than titanium [31]. The corrosion of magnesium changes the pH of surrounding environment due to the release of OH^- ions. This pH increase inhibits enzyme activities important to bacteria [30].

The major drawback of magnesium as a very reactive metal is its low corrosion resistance. Magnesium can corrode too quickly, losing mechanical integrity before the tissue has sufficiently healed [11]. By appropriate alloying as well as surface treatments and coatings, corrosion resistance of magnesium can be improved [26, 27]. The mechanical strength can be customized as well according to the alloying elements [33, 35]. However, especially alloys with high dissolution rates, are linked to cytotoxicity due to the release of alloying metal ions [36].

Zhang et.al. studied a biodegradable Mg-Zn alloy. The addition of zinc elevated the corrosion potential of magnesium and resulted in a reduction of the degradation rate. Moreover, the alloy showed suitable mechanical properties and no adverse effects caused by the release of zinc [34].

2.4 Mg2Ag

Silver is well known in medical application for its antibacterial property [31, 32]. Mg-Ag alloys proved to reduce the viability of pathogenic bacteria and thus solve the infection problem around implants [31]. In vitro tests showed negligible cyto-

toxicity for low concentrations of silver and a good cytocompatibility [37, 38]. In fact, the released silver concentration in Mg2Ag was low enough to not be cytotoxic, but high enough to show antibacterial activity [31].

Furthermore, mechanical and corrosion properties can be adjusted depending on heat treatment and Ag-content. Increasing silver content leads to a higher corrosion rate due to galvanic corrosion which, however, can be improved by heat treatment to values lower than for pure magnesium [31]. The decrease of the corrosion rate with no additional toxicity by the presence of silver and inhibiting the adhesion of bacteria make Mg2Ag an interesting alloy for biomedical applications [31].

2.5 Mg-Ti

The Mg-Ti phase diagram is shown in figure 2. There is very low mutual solubility and no intermetallic phases occur in the system.
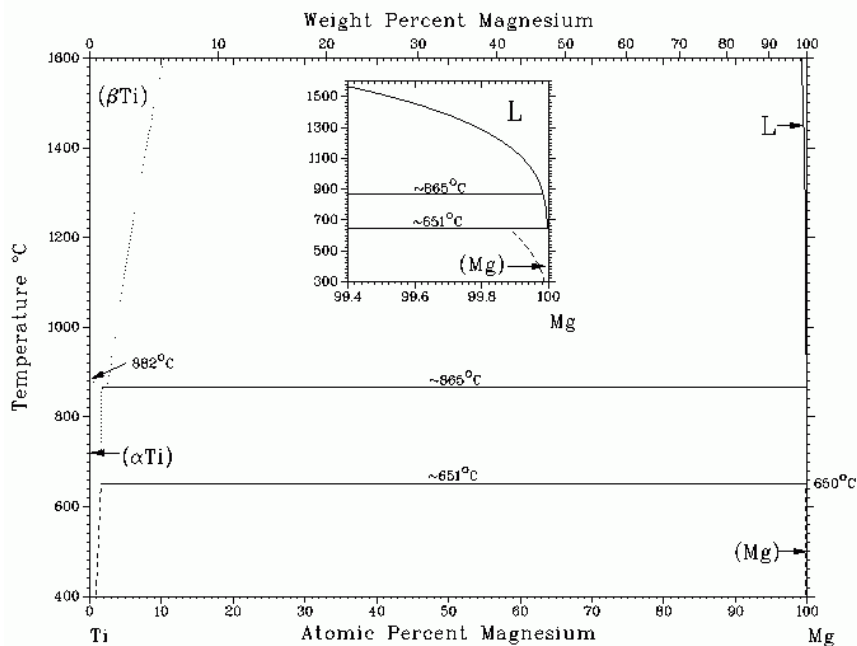
Figure 2: Mg-Ti phase diagram [39]

However, metastable Mg-Ti alloys were successfully synthesized by non-equilibrium

processes. The solubility of titanium in magnesium was thereby extended substantially. The thermal stability of these supersaturated solid solutions is low: Decomposition starts at temperatures as low as 200°C [40]. With the development of nanocrystalline alloys the stability could, however, be increased by pinning the grain boundaries and retarding grain growth [40]. Various techniques were used to produce Mg-Ti alloys:

- Mechanical alloying successfully produced magnesium-based and titanium-based alloys. The corrosion rate could be reduced and the alloys proved to be non-cytotoxic [40].

- Vapour quenching: By evaporation of titanium and magnesium from separated sources and mixing the vapours before condensation Zheng et.al. produced a Ti-29 wt.%Mg alloy, whereby some Ti-rich and Mg-rich regions appeared [41].

- Ball milling: In a repetition of plastic deformation and mix of the raw materials magnesium dissolves in titanium and stabilizes the BCC phase by introduction of stacking faults. The larger magnesium impedes the grain boundary diffusion of titanium and stabilizes thus the BCC phase thermally [42].

- Magnetron sputtering: A single-phase Mg-Ti alloy with a wide composition range was produced. The corrosion resistance could be increased with increased Ti content. Complete passitivity was reached only when the alloy became titanium-based with the formation of a protective surface film. This technique offers the possibility of surface alloying to passsivate magnesium without changing the bulk composition and properties [43].

- Garcés et.al. studied Mg-12 wt.%Ti alloys obtained by physical vapour deposition and characterized microstructure and precipitation behaviour upon annealing [44, 45].

The combination of magnesium and titanium has several advantages: The elastic modulus and the associated stress shielding are reduced. The high corrosion rate of magnesium can be reduced as well, a major concern for the application of

magnesium as an implant material. Furthermore, degradation of magnesium can produce a porous titanium which facilitates the bone in-growth and the anchoring between bone and implant [46].

2.6 Electron beam welding

The electron beam welding (EBW) technique is based on the interaction between highly accelerated electrons with the material to be welded. Electrons are emitted by a heated electrode (usually a tungsten electrode heated by current) and accelerated by an applied voltage. Very high electron speeds are thereby achieved: For 150 kV electrons reach about 63 percent of the speed of light [47]. A Wehnelt electrode is used to control the beam current density. To direct the electron beam to the specimen surface, magnetic coils are used to focus the electrons and to alter the focal length. The deviation of the beam on the work piece is obtained by arranging two coils perpendicular to the electron beam with a second set of coils rotated by 90 degrees allowing deviation in the other direction. Further magnetic coils make it possible to change the shape of the beam cross-section to a desired form or to correct astigmatism. The use of magnetic fields allows very fast control compared to mechanical control. A vacuum system has to be installed to prevent the widening of the electron beam by scattering on gas atoms [47].

When the electron beam hits the surface, collisions with atoms transfer the kinetic energy from the electrons to the atoms increasing their temperature. The penetration depth depends thereby on the accelerating voltage and the density of the specimen and is usually less than 0.1 mm. However, the temperature increase leads to melting and partial vaporisation of the material producing the so called deep penetration effect, the basis of electron beam welding: A vaporisation of the material in the centre of the beam leads to the creation of a capillary hole (keyhole) by vapour pressure, allowing the electron beam to penetrate deeper into the material. Hence, large welding depths up to 200 mm in steel are possible [47].

Electron beam welding is especially useful, as it produces very narrow weld beads and the heat affected zone is a lot smaller than for conventional welding techniques, while the welds demonstrate high strength. Because of the small beam diameter very high energy densities are reached, enough to vaporise the metal and

(a)   (b)
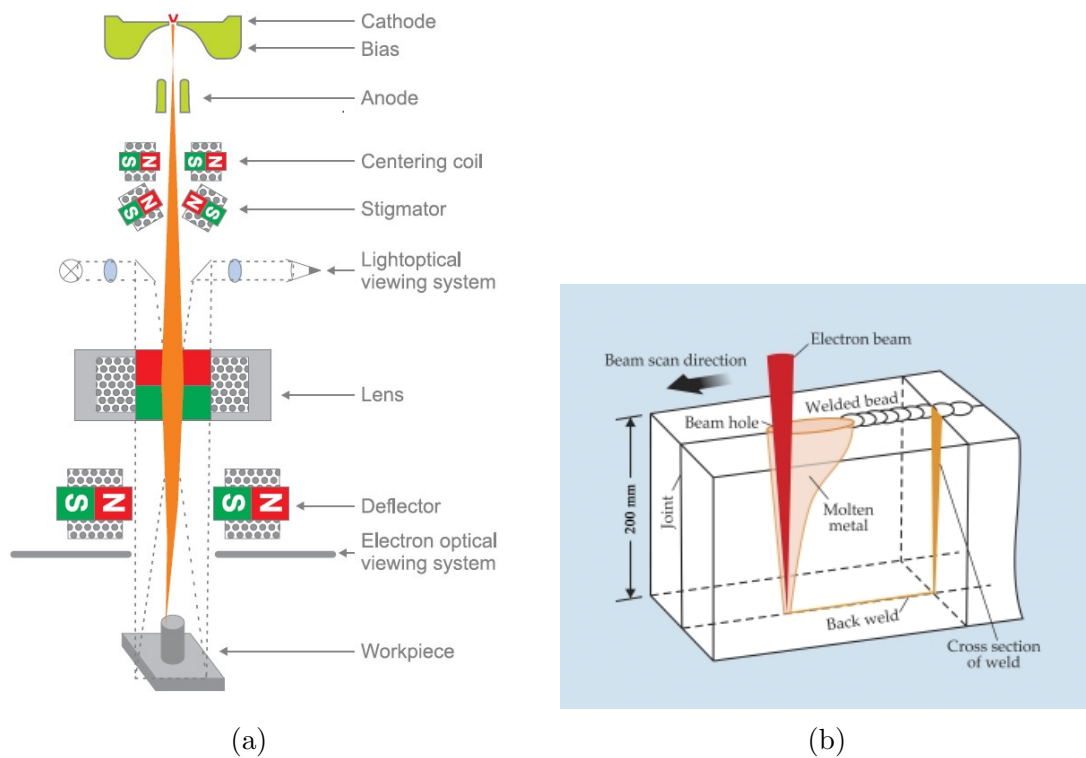
Figure 3: Functioning of an electron beam welding machine: (a) schematic display
          [47] and (b) deep penetration effect [48].

to produce very deep welds. The big advantage of EBW is that it can be deflected
nearly inertia-less and very precisely on different, also complex deflection figures
with chosen frequencies and the attainment of high welding velocities. Electron
beam welding can also be carried out using a filler metal. Disadvantages of this
technique are the required vacuum system and the high energy consumption of the
process.

2.7 Aim and motivation

The purpose of this work is to produce the joining of two dissimilar metals for
potential medical application. Both titanium and magnesium have advantageous
properties and are successfully employed in implant technology. The processed
material will combine the advantages of both materials: the bioactivity and the
elastic modulus closer to bone of magnesium and the specific strength of titanium

in comparison with other biometallic materials. Coatings of magnesium on titanium using physical vapour deposition [49] and joining of magnesium and titanium with ultrasonic spot welding have been performed to create supersaturated Mg-Ti alloys [50]. However, no studies with electron beam technique are known to be conducted for this kind of joint.

The feasibility to create a joint between titanium and magnesium with electron beam welding and the correlation of welding parameters with microstructure, surface finish and interface quality are the topics of investigation in the present work.

3 Experimental

3.1 Materials

3.1.1 Magnesium

Commercial pure magnesium and a Mg-Ag alloy with two weight percent of silver (Mg2Ag) were used in the present work. The physical, mechanical and thermal properties of pure magnesium are set out in table 1. These two materials were chosen based on their favourable characteristics as implant materials stated in section 2.3 and 2.4. Both have low density and high strength, comparable to the human bone plus good biocompatibility. Mg2Ag has the additional asset of antimicrobial behaviour and the option to form precipitates, thereby changing microstructure and mechanical properties.

Table 1: Physical, mechanical and thermal properties of magnesium [51]

Property	Value
Density	1740 $kg/_{m^3}$
Young's modulus	44.0 GPa
Melting point	650 °C
Boiling point	1090 °C
Specific heat capacity	1025 $J/_{kg\ K}$
Thermal conductivity	159 $W/_{m^{-1}\ K^{-1}}$
Coefficient of thermal expansion [T = 20 - 100 °C]	$26.1*10^{-6}$ K^{-1}

Figure 4 shows the phase diagram of the binary alloy Mg-Ag and the position of Mg2Ag within the diagram. The solid solubility of Ag in Mg solution is 3.83 at.% at the eutectic temperature of 472°C. In equilibrium at 2 wt.% silver content the alloy is in a two-phase region with one phase being magnesium (with little silver in solid solution) and the other intermetallic Mg_4Ag.
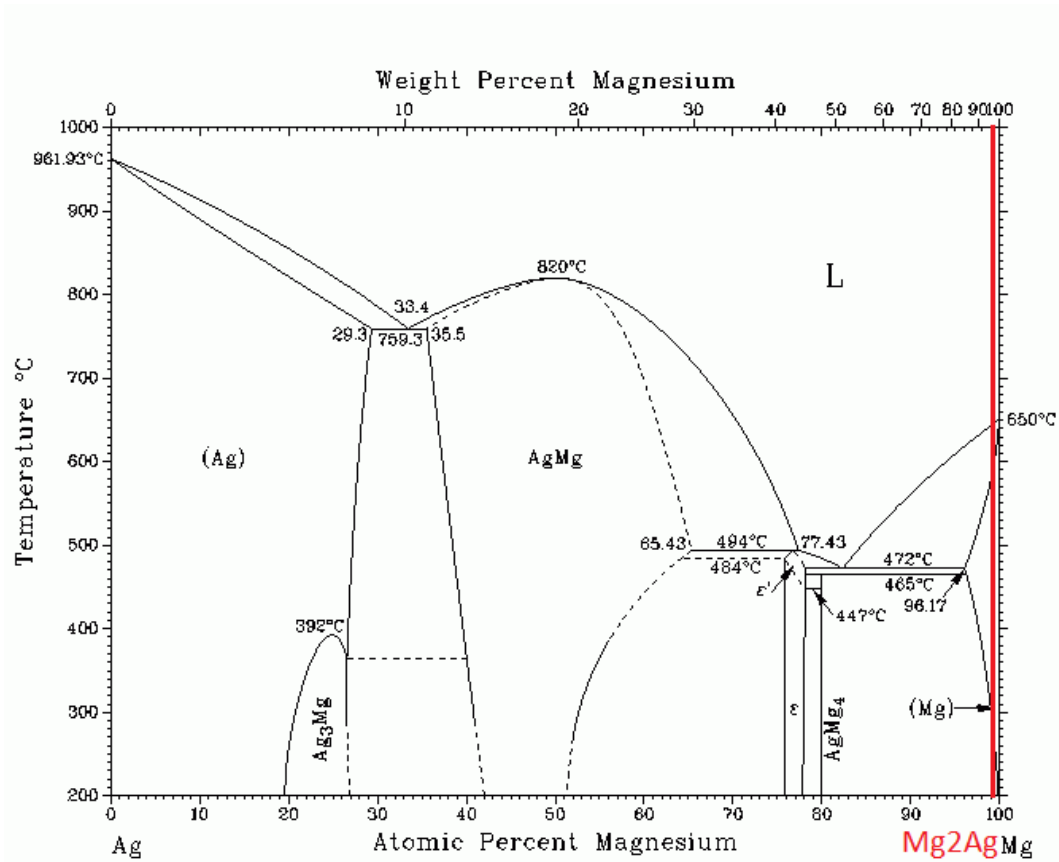
Figure 4: Ag-Mg phase diagram [39]

3.1.2 Titanium

Titanium Grade 2 was used as the base material. Titanium Grade 2 is an un-alloyed, medium strength titanium product with good weldability and corrosion resistance. Its use in medicine is well-established. The composition is given in table 2 and its physical, mechanical and thermal properties in table 3.

Table 2: Composition of titanium Grade 2 [52]

Component	Wt. %
C	Max 0.1
Fe	Max 0.3
H	Max 0.015
N	Max 0.03
O	Max 0.25
Ti	99.2

Table 3: Physical, mechanical and thermal properties of titanium [52]

Property	Value
Density	4510 $kg/_{m^3}$
Young's modulus	105 GPa
Beta Transus temperature	913 ℃
Melting point	Max 1665 ℃
Specific heat capacity	523 $J/_{kg\ K}$
Thermal conductivity	16.4 $W/_{m^{-1}\ K^{-1}}$
Coefficient of thermal expansion [@ T = 20 ℃]	$8.6*10^{-6}$ K^{-1}

3.2 Experimental setup and sample preparation for EBW

Magnesium was cut into square plates (15x15 mm^2) of a thickness ranging from 0.25 to 1 mm with a Struers Accutom2 cutting device using a silicon-carbide cut-off wheel (10S15) while cooling it with water. The titanium plates were already cut into 15x15 mm^2 plates with a thickness of 1 mm or 2 mm. Before assembling the Mg-plates and the Ti-plates both were ground with #4000 grinding paper to obtain surfaces that enable a good contact between the two metals. The two plates were cleaned ultrasonically and assembled with the aid of a clamping device (see figure 5).
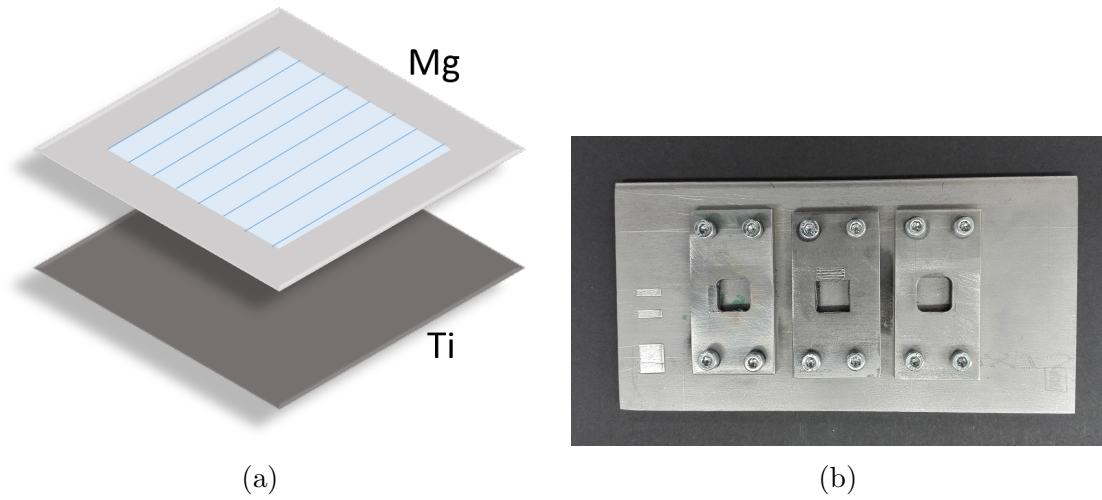
Figure 5: Experimental setup: (a) schematic representation of experimental design and (b) clamping device.

3.3 EBW experiments

Electron beam welding was used to join the two metals. The EBW machine EBG 45-150 K14 (see figure 6) is suitable for a wide range of application. Due to its high beam power of up to 45 kW almost all metals and many material combinations can be welded. Vacuum system, motion of the welding table and beam deflection are controlled by numerical control (NC). The technical parameters and their range are given in table 4.

Table 4: Technical data of the EBW machine EBG 45-510 K14

Property	range
Power	Max 45 kW
Voltage	60 - 150 kV
Beam current	0.1 - 300 mA
Travel speed of the welding table (in x and y)	Max 100 mm/s
Frequency	1 - 65535 Hz
Welding time	
Deviation figure size (in x and y)	-100 - +100 mm

Before starting the actual welding process, the electron beam needs to be set up:

Figure 6: pro-beam electron beam welding machine K14

The filament peaking routine is performed at a current higher than later used in the experiments. Then the electron beam needs to be adjusted to define optimal centering and stigmatization values. Furthermore, for each used electron beam current the focus current needs to be determined. Finally the electron beam deflection needs to be calibrated: Depending on the accelerating voltage and the distance between work piece and deflection coils a calibration factor is identified which is unique for each work piece and needs to be incorporated into the NC welding program. Then the starting position is approached and the program can be started.

The ideal parameters for the welding process were identified performing several steps: Firstly, blind-welds were produced varying welding speed (from 40 mm/s to 60 mm/s) and current (from 1 mA to 3 mA). In this case the electron beam was stationary while the welding table was moved. Suitable welding speeds and beam currents were determined from the blind welds that produced a joining between magnesium and titanium and used for further experiments.

For all subsequent experiments the beam was deflected with the welding table staying fixed. The welding was now carried out using deviation figures to create a two-dimensional joint. Some of the parameters had to be adapted as the proximity

of the welding points influenced the outcome of the weld. The welding parameters given in table 5 with their tested range were then improved progressively following microscopic analysis.

Table 5: Experimental parameters for setup, electron beam and beam figures with used value or range

Parameter	value or range
Mg-plate thickness	0.25 - 1 mm
Ti-plate thickness	1 - 2 mm
voltage	150 kV
current	1 - 3 mA
focus	-10 - 0 mm
beam figure	lines, grid, random points
point density	50 pts/mm
line spacing	0.25 - 1 mm
energy input	3 - 25 J/mm^3
beam velocity	40 - 400 mm/s
frequency	1000 - 20000 Hz
welding time	0.5 - 5 s

The NC program reads the previously created deviation figure file where each point is given by an x- and y-coordinate and the electron beam is deflected accordingly. The actual dimensions of the deviation pattern on the sample needed to be entered as well as the beam current and the focus current. The shape of a single spot used in the present work was a fine point to which the electrons were focused by the focusing lenses. The read rate (frequency) determines the number of points targeted per second and defines (together with the length of the file containing the coordinate points) the required time for one full swipe of the deflection figure. The welding time can further be set to fix the number of swipes.

Depending on the point density along a welding line, the frequency was chosen accordingly to reach a certain beam velocity: For a point density of 50 pts/mm and a frequency of 10000 Hz, the beam velocity is 200 mm/s. Similarly the energy input into the sample can be calculated and adjusted. The energy depends on the used current, voltage and welding time.

The deviation figure was defined to be 10x10 mm^2 in size and the accelerating voltage was kept constant for all weldings at 150 kV. By changing the focus current

the beam can be focused on any point within the sample. As a consequence the impact area on the sample surface, where the converging beam is still defocused, is increased.

Also the NC control allows a preheating and a post weld heat treatment of the sample: By means of a tacking routine, where the parameters can be chosen similar to the welding process, the sample can be preheated. This is usually performed with lower current and/or higher frequency. In the present work, the same deviation figure was used for the tacking and welding procedure. The same applies to the smoothening routine which carries out a post weld heat treatment. The waiting time between preheating and welding, and welding and postheating can be chosen as required.

3.4 Beam figures

The beam deflection pattern is freely programmable in a matrix of 65535x65535 points. Each figure consists of a certain number of points defined by x- and y-coordinates in this matrix. MATLAB was found to be a suitable program to create the input data. The compiled MATLAB code can be found in the appendix.

The MATLAB script was designed to create different structures by providing the corresponding input parameters. By entering the dimension of the final deviation figure of the sample, 10x10 mm^2 in the present work, all other pattern dimensions can be entered in mm as well. On the MATLAB interface the arrangement of the points in the beam figure can be selected (either a line-type, grid-type or random points). For the line-type and grid-type deviation figures the point density along a line (how many points per mm) and the distance between the single welding lines can be chosen. The line spacing should be small enough in order to get an overlapping of adjacent welding lines. For the random-point-type the number of points need to be defined which are then created randomly in the 65,535x65,535 matrix.

The generated file is displayed in a figure to visualise the result immediately (examples of deviation figures can be found in figure 7). Furthermore, an output file is created that is subsequently imported into the NC. This file consists of the x-

and y-coordinates of the single points. After transferring the file to the NC it was read line by line and the points were targeted sequentially.

(a)   (b)
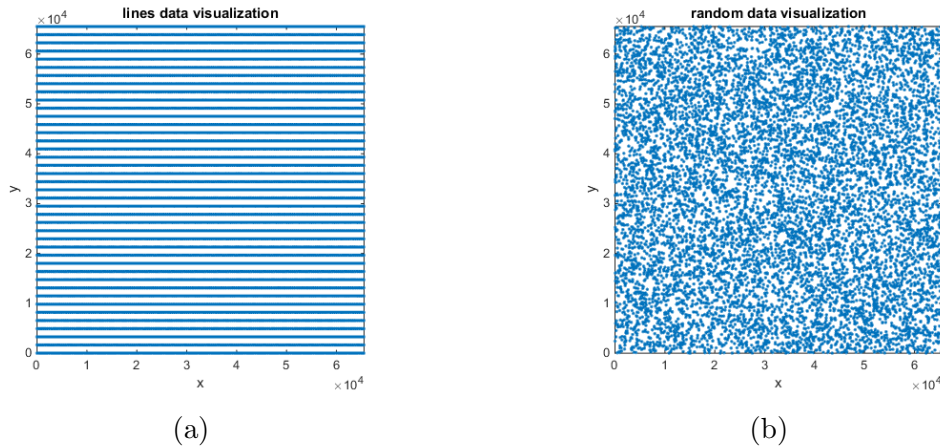
Figure 7: Deviation figures created by MATLAB: (a) line-type (point density: 50 pts/mm; spacing: 0.25 mm), (b) random points (10000 points).

3.5   Metallography

3.5.1   Grinding and polishing

The samples were cut in half after welding and ground and polished. These steps were performed with a STRUERS Tegramin-30 semi-automatic preparation system. The grinding times and grit sizes are listed in table 6. The force was set to 10 N per sample. Between each grinding step the samples were rinsed with water to prevent particles to be transported on the successive grinding paper and potentially introduce severe scratches.

After the last grinding step and between each polishing step the samples were cleaned ultrasonically for 3 minutes. Also, the samples were only rinsed with ethanol after grinding to prevent corrosion of the surface. The polishing times and consumables are listed in table 6. These grinding and polishing times were prolonged or repeated as required (mainly for #4000 paper and polishing with OP-S). To remove the polishing agent OP-S the nap was rinsed with ethanol for the last minute of polishing and furthermore the samples were cleaned on an extra nap solely with ethanol. This was necessary because especially at the interface a lot of

OP-S got stuck which made an examination of the interface impossible. Titanium has a lower polishing rate than magnesium which leads to a difference in height between the two metals making the polishing agent hard to remove.

Table 6: Grinding and polishing grit sizes and preparation times

Grit size	time [min]
500	4
800	4
1200	4.5
2000	4.5
4000	2x3
MD-Nap with 1 µm DiaDuo-2 (diamond suspension)	10
MD-Chem with OP-S (colloidal silica suspension)	2x10

3.5.2 Etching

To analyse the microstructure, the samples were etched either with Nital or with a mixture of acetic and picric acid for the investigation of magnesium and with hydrofluoric acid for titanium. Both etching agents for magnesium produced acceptable results. The compositions and etching times are specified in table 7.

Table 7: Composition of etching agents and immersion times

Etching agent	composition	etching time [s]
Mg: Nital	100 ml ethanol 3 ml nitric acid (65%)	60 - 120
Mg: picric acid	5 ml H_2O 70 ml ethanol 5 ml acetic acid 2.1 g picric acid	2
Ti: hydrofluoric acid	100 ml H_2O 5 ml H_2O_2 (30%) 2 ml HF (40%)	30 - 60

Investigation of microstructure, defects and interface were then carried out by

light optical microscopy (LOM) and scanning electron microscopy (SEM). Energy-dispersive X-ray spectroscopy (EDX) was used to identify the element distribution at the interface and within the Mg2Ag alloy.

3.6 Heat treatments

After electron beam welding heat treatments were carried out for the Mg2Ag alloy in order to release internal stresses after fast cooling and to precipitate second phases.

All heat treatments were performed in a Nabertherm P330 oven. The temperature in the oven was kept stable during the ageing process with the aid of a 2 kg steel block. The oven was preheated to the desired temperature and the samples were introduced as soon as the temperature stabilised.

First, a solution heat treatment was carried out: 450 ℃ for 24h and then quenched in water. Similarly a solution heat treatment was performed for 2 hours and subsequently cooled in air by placing the samples on a ceramic block and left to cool to room temperature. Also, an ageing treatment was run straight after the welding process at three different temperatures (180 ℃, 200 ℃, 220 ℃) and for different times (1, 2, 4, 8, 24 h) with subsequent air cooing.

The samples were ground and polished for hardness measurements and observation in the scanning electron microscope. Furthermore, the evolution of the microstructure during heat treatment was observed after etching.

3.7 Hardness measurements

Hardness measurements were performed both in titanium and magnesium. Magnesium is known for its soft properties and hardness measurements are often difficult. Indeed, macrohardness measurements did not result in usable indents. Therefore microhardness was measured. The Anton Paar MHT4 microhardness tester was used with a pyramidal diamond indenter with an interfacial angle of 136° to obtain Vickers hardness values. The parameters for the hardness measurements were as follows:

- Force: 100 ponds

- Holding time: 15 seconds

- Force increment: 2 ponds/second

Each sample was measured 7 times in order to determine an average value.

To be able to measure the hardness of smaller details in the magnesium-silver alloy (since a force of 100 ponds produced an indent with diagonals in the order of 60 µm), some measurements were performed with a force of only 10 ponds while keeping the other parameters constant. Vickers hardness measurements followed certain standards: For a single measurement to be valid, the ratio between the diagonals needs to be larger than 0.96. All indents with higher distortion were discarded.

3.8 Characterization of the surface

The topography was studied by scanning electron microscopy, stereo microscopy and with Alicona InfiniteFocus.

The surface finish of an implant is of vital importance as this is where the contact between body cells and metal happens. Firstly the magnesium surface is the critical constituent as it is corroded by the body environment. When, however, the magnesium is dissolved completely, the permanent implant material titanium comes into play, with osteoblast attachment to the titanium surface, on which the roughness has an important impact.

Therefore, the surface needs to be defined as clearly as possible. There are various standardised parameters which can be determined from a surface measurement. For the present work the following roughness parameters were found to be the most useful for describing the surface:

- R_a (arithmetic average roughness): takes the arithmetic average of the height from the mean line

$$R_a = \frac{1}{l} \int_0^l |z(x)| dx \tag{1}$$

  where l is the sampling length, z the distance from the mean line and x the coordinate along the sampling length

- R_q (geometric average roughness): takes the arithmetic average of the height from the mean line

$$R_q = \sqrt{\frac{1}{l} \int_0^l z^2(x)dx} \tag{2}$$

- Increment of surface: ratio between real and projected surface

- Roughness depth

R_q amplifies occasional highs and lows and therefore complements R_a which is less sensitive in this regard. The R_a roughness may give the same results for an evenly rough surface and a flat surface with larger occasional irregularities, while the R_q roughness takes these irregularities into account. By comparing the two values, some conclusions of the shape of the profile can already be made.

In addition, the increment of surface gives an idea how much additional surface was created with electron beam welding compared to a flat surface. By measuring the height differences between a peak and the adjacent valley in the primary profile, the mean profile depth can be determined.

(a)   (b)
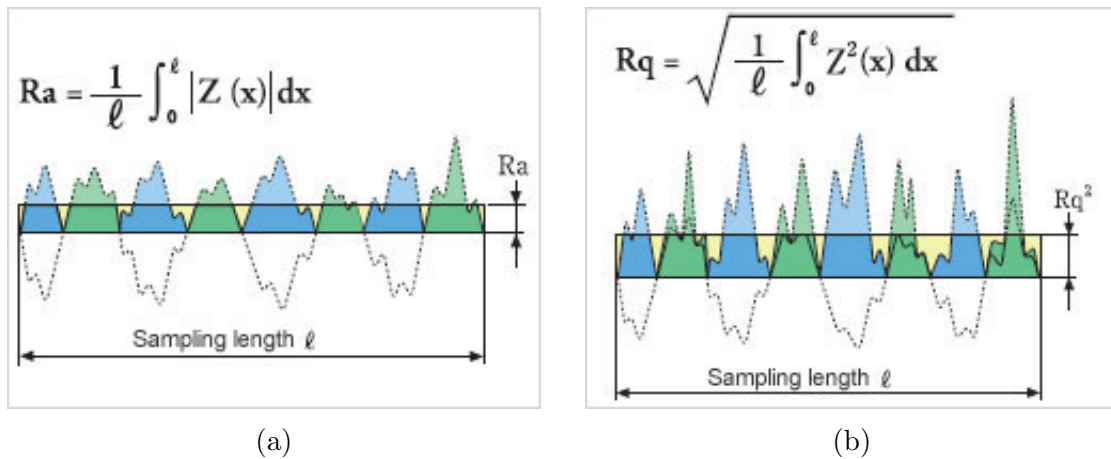
Figure 8: Definition of roughness parameters [53]: (a) arithmetic average roughness R_a (b) geometric average roughness R_q.

To be able to examine the titanium surface below the magnesium, the samples were deep-etched with HNO_3 20 vol.%- EtOH 80 vol.%. After about 7 hours the

whole magnesium was removed without affecting the titanium, which has a good corrosion resistance in nitric acid.

3.8.1 Alicona measurements

To assess the roughness of the surface, Alicona measurements were performed. Alicona is an optical, non-contact measuring device which provides topographical and colour information by variation of focus. It produces a three-dimensional picture of the surface by measuring optically stepwise from the lowest elevation in the profile to the highest and determining at which height the surface is in focus. The vertical resolution depends on the objective magnification being as low as 10 nm for a 100-fold magnification. The program allows to analyse the sample surface as well as roughness along a defined line.

The roughness of the titanium surface was measured both perpendicular and parallel to the welding lines. In the latter case, roughness was determined on the ridge, in the groove as well as halfway between the two. The width of the line, along which the roughness was determined, was defined in order to get an average profile within this width to even out large irregularities and to get a representative roughness. For the lower 10-fold magnification a line width of 30 µm was used while for the 100-fold magnification the line width was reduced to 3 µm.

The primary profile was filtered with a defined wavelength distinguishing between waviness and roughness of the surface. This cut-off value (λ_c) defines the largest wavelength that is included in the roughness. Longer wavelengths are filtered out and included in the waviness (compare figure 9). From surface pictures superimposed by height information the cut-off wavelength was adjusted to a reasonable value, where waviness and roughness were coherent with the actual surface of the sample. This value was found to be 80 µm.

To be able to compare different roughnesses the cut-off wavelength needs to be the same. If λ_c is increased, more surface irregularities are attributed to roughness and less to waviness. This would increase the roughness and decrease the waviness making values with different λ_c incomparable.

Similarly, the magnesium surface after EBW was studied with Alicona: The in-
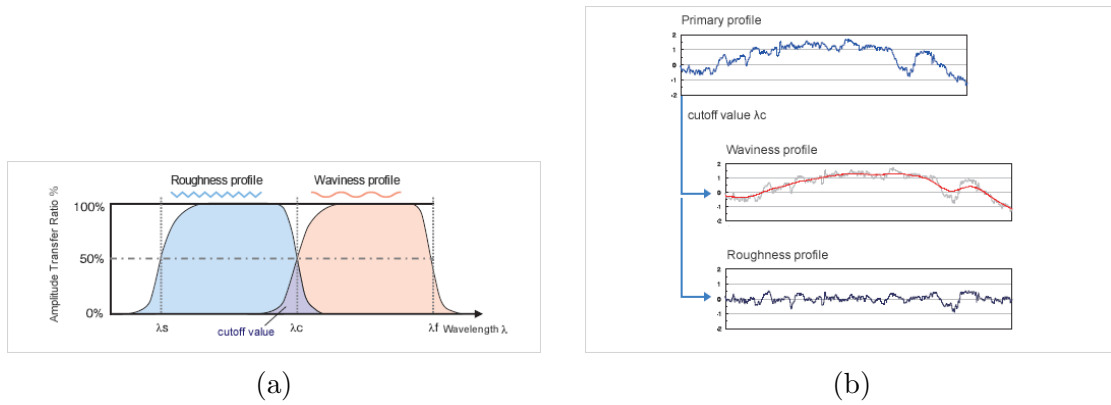
Figure 9: Division of the primary profile into waviness and roughness by applying the cut-off value λ_c [53]: (a) cut-off value λ_c (b) primary profile and respective waviness and roughness profiles.

crement of surface was recorded and the roughness and waviness perpendicular to the welding direction were evaluated as well as the roughness depth.

4 Results and discussion

4.1 Microstructure

4.1.1 Magnesium

The microstructure of commercial pure magnesium is depicted in figure 10. It consists of large grains up to 3 mm in diameter with some twinnings provoked by cutting and polishing. Twins are frequently formed in hexagonal close-packed (HCP) metals in order to dissipate energy [54].

Z2m Mikroskopvergrößerung: 62,5x; Bildbreite: 2231,26 µm

Bildname: biomat16_d0038.jpg
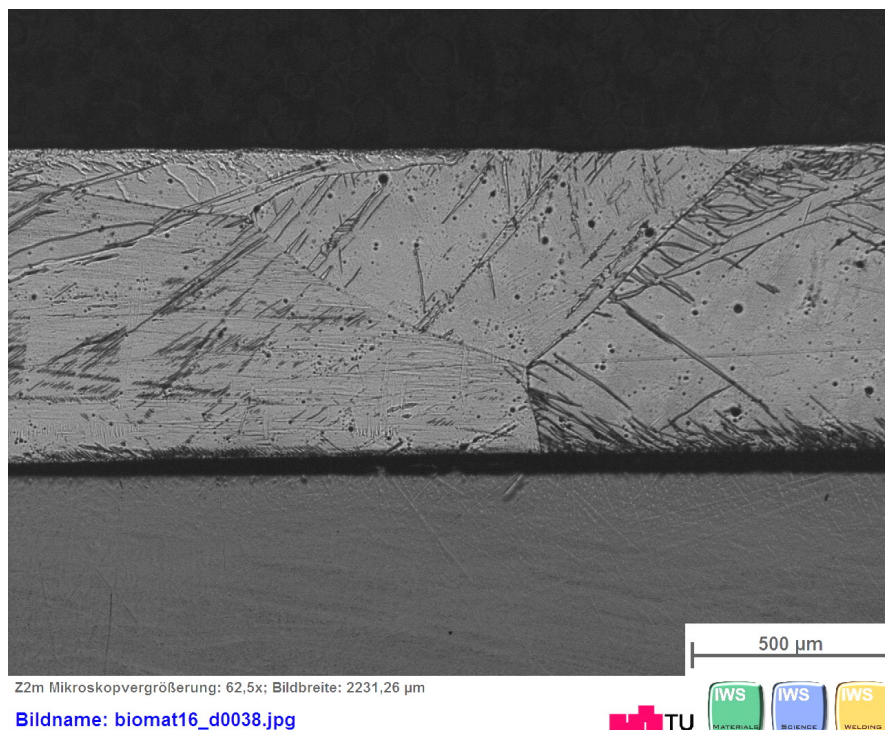
Figure 10: Microstructure of pure sand cast magnesium (LOM image, etched with Nital)

4.1.2 Mg2Ag

As seen in section 3.1 Mg2Ag is in a two-phase region in equilibrium. However, casting is a non-equilibrium process and results in the case of Mg2Ag in a dendritic structure as shown in figure 11. During solidification microsegregation occurs and

as a consequence the concentration of the solute silver is not constant throughout the casting. The reason for this segregation is the first solid formed being very low in silver concentration. When the temperature is lowered and reaches the liquidus temperature the stable solid phase is nearly 100% magnesium according to the lever rule. This solid phase starts to grow in dendrites. The liquid phase is now enriched in silver and a redistribution of silver will take place as the dendrites continue to grow. Finally, the silver-enriched liquid solidifies in between two dendrite arms. In an equilibrium state, slow cooling prevents this segregation as silver is incorporated slowly into the magnesium-rich solid by diffusion. For castings, however, the cooling rate is too fast and as the diffusivity drops exponentially with temperature, the silver atoms do not have enough time to diffuse.
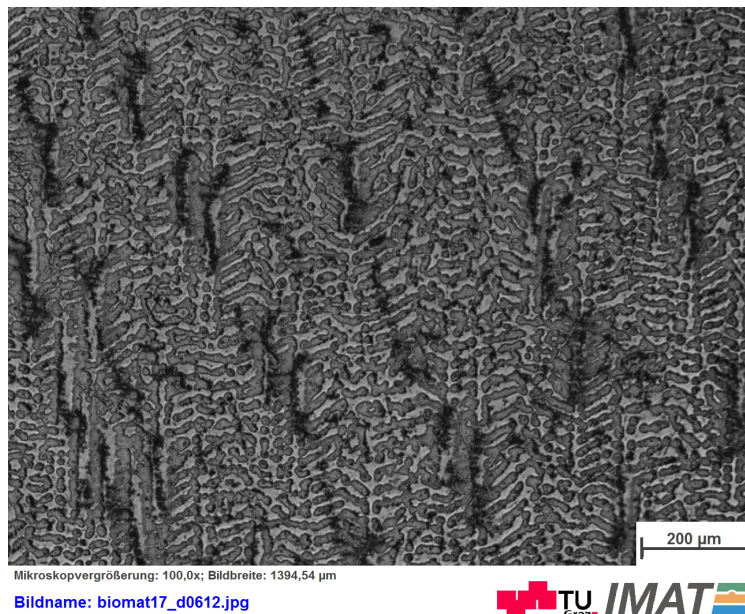
Figure 11: Dendritic structure of the Mg2Ag-alloy
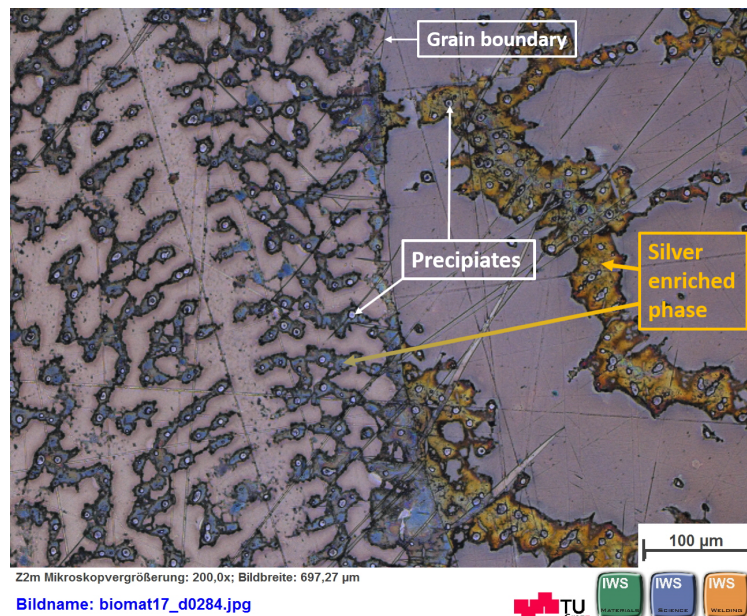
Figure 12: Mg2Ag microstructure as cast

Figure 12 shows a detail of the Mg2Ag microstructure: In the centre a grain boundary is visible as well as some twins. Silver-rich volumes of various sizes are arranged in between the dendrite arms and some precipitates in the order of a few micrometres in diameter are found within the enriched volumes.

4.1.3 Titanium

The used titanium Grade 2 had been thermomechanically processed. The microstructure consists of equiaxed grains of about 50 µm in diameter.

Mikroskopvergrößerung: 200,0x; Bildbreite: 697,27 µm

Bildname: biomat17_d0661.jpg
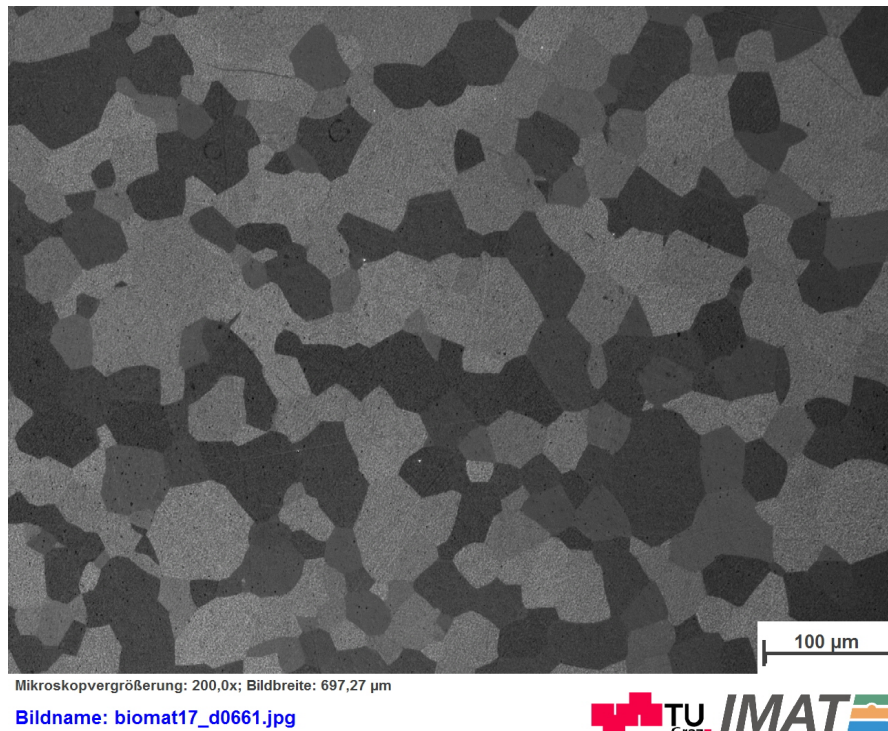
Figure 13: Titanium Grade 2 microstructure

4.2 Blind welds

The structure of a single blind weld bead for a welding velocity of 50 mm/s and
a current of 2 mA can be seen in figure 14. The melting zone is about 400 µm
wide on its smallest point and wider at the magnesium surface and the Mg-Ti
interface. The shape of the melting zone may be a consequence of the difference
in heat dissipation: In the centre of the magnesium more surrounding volume is
available for heat dissipation than on the surface. At the interface thermal contact
resistance and the lower thermal conductivity of titanium (compare table 1 and
table 3) deteriorate heat dissipation. Furthermore, close to the magnesium surface
and at the Mg-Ti interface some smaller grains can be found which are a result of
working (essentially cutting) of the plates.

In the centre of the weld, where the electron beam primarily interacts with the
material, smaller grains are present contrasting with the large grains of the base
material. These grains are the result of microstructural changes induced by the
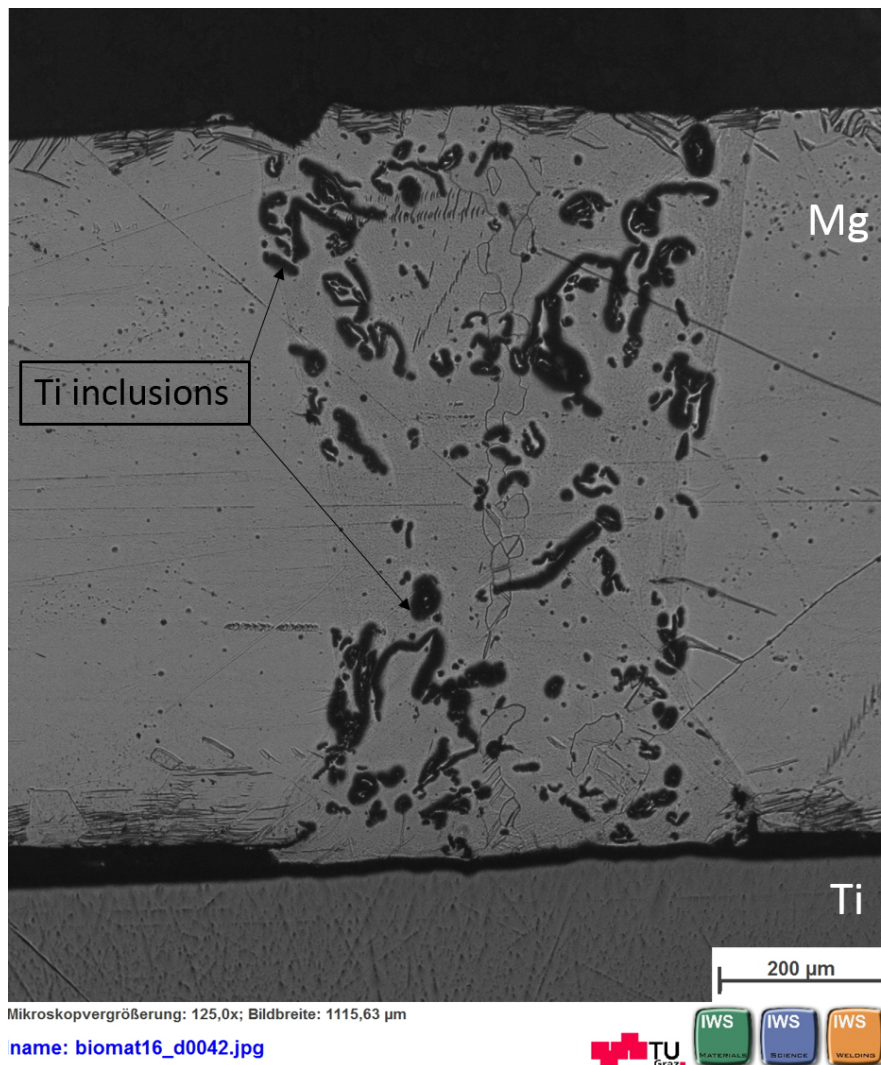
Figure 14: LOM image of a single blind weld etched with Nital (I = 2 mA, v = 50 mm/s, focus = -2 mm)

welding process and are about 35 μm in width and oriented parallel to the weld bead. Their dimension parallel to the weld bead varies and they do not appear over the entire depth of the weld. These small grains are the consequence of rapid solidification upon cooling. Furthermore, on the edge of the fusion zone the grain boundaries reoriented (for example for twin boundaries crossing the fusion line).

Titanium inclusions are found in the molten magnesium weld bead. As described

in section 2.6 local evaporation leads to the formation of a cavity through which the electron beam can penetrate deep into the material and eventually reach the interface. There some small titanium particles are detached from the bulk and by heat induced convection incorporated into the molten magnesium where they are fixed upon solidification. The inclusions are mostly threadlike and whirled or branched with some of them forming larger three-dimensional particles (see figure 15).

(a)   (b)

(c)   (d)
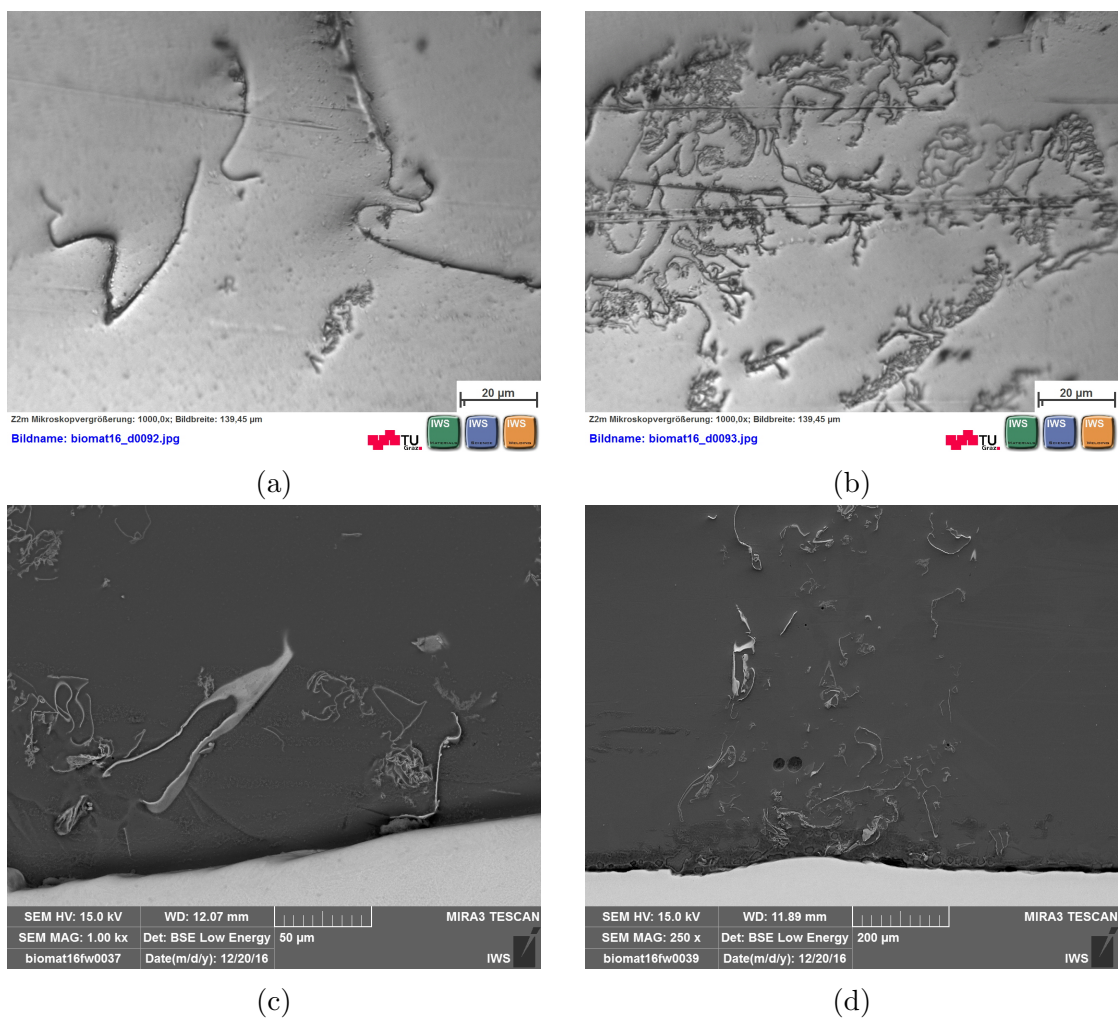
Figure 15: Example of titanium inclusions within the magnesium matrix: (a) - (d) frequency = 2000 Hz, line spacing = 1 mm, defocus = 5 mm.

The blind welds were performed with velocities ranging from 40 to 60 mm/s. The lower the welding speed, the more titanium inclusions are found in the melting area. A slower welding speed increases the energy input and thus provokes a higher melting fraction of titanium (see figure 16).

(a)	(b)
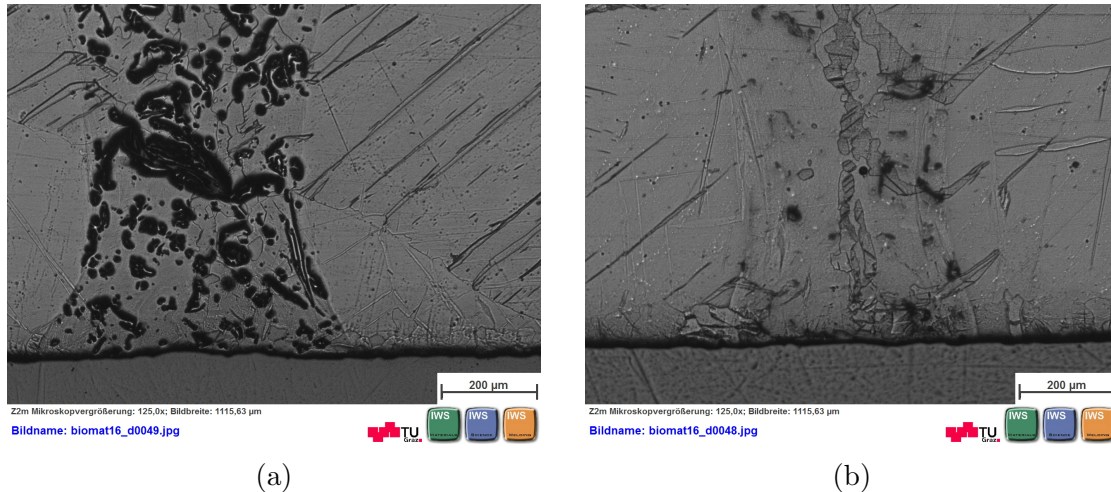
Figure 16: Influence of the welding speed on the amount of titanium inclusions (LOM image, etched with Nital; I = 2 mA, defocus = 2 mm) : (a) v = 40 mm/s; (b) v = 60 mm/s.

The beam current was varied from 1 mA up to 3 mA. For 1 mA and 1.5 mA the beam penetration depth was too low to form a joint because the beam did not reach the interface at all or only barely (see figure 17). 3 mA produced a joint but the energy input was too high, melting high portion of the sample and moving a considerable amount of material often exposing the titanium surface as will be explained later.
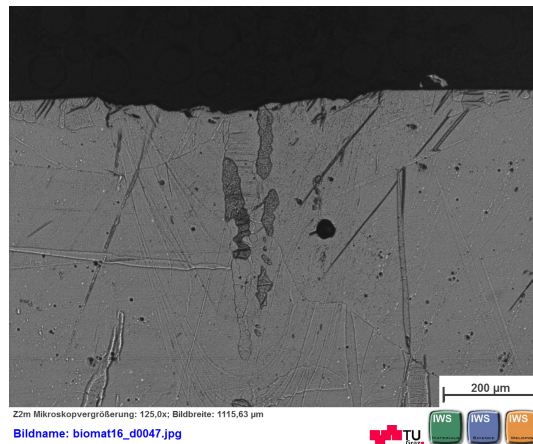
Figure 17: Melting zone for a welding current of I = 1.5 mA (LOM image, etched with Nital; v = 50 mm/s, no defocusing)

4.3 Optimization of EBW-parameters

In order to approach an optimal outcome of the two-component system the welding parameters were varied one by one and the results analysed taking into account the following criteria: formation of a joint interface over the whole area, reduction of microporosity, removal of macroporosity and cracks and a good surface finish. Consequently, the parameters were adjusted accordingly.

4.3.1 Influence of beam focus

The focus of the electron beam can be altered by changing the lens current. Consequently, the point with the smallest beam diameter and hence the maximum power density can be varied vertically through the sample. Instead of focusing the beam on the magnesium surface, the focus can be placed on any point within the sample. This changes the surface finish of the sample: The lower the focus point, the wider is the area affected by the beam on the sample surface and more material is moved. As a result, the surface roughness increases. Figure 18 shows the magnesium surface of three samples welded with the same parameters and solely changing the focus. The more the beam was defocused towards the sample interface, the broader were the welding lines on the surface. However, a change of focus did not have a large impact on the quality of the joint itself. Therefore,

focus was kept constant (with the focus point on the surface of magnesium) for all subsequent experiments.
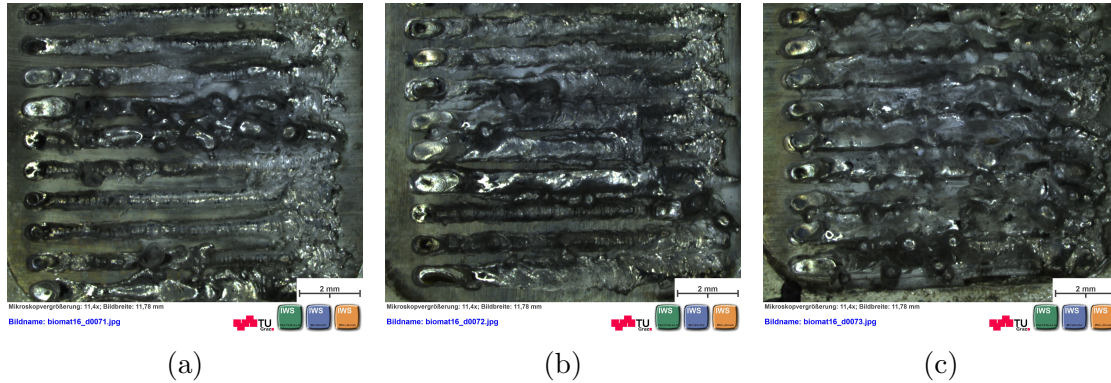
Figure 18: Influence of focusing on surface finish for a line-type beam figure (I = 2 mA, frequency = 2000 Hz, line spacing = 1 mm): (a) no defocusing; (b) defocus = 5 mm; (c) defocus = 10 mm.

4.3.2 Influence of the beam figures

The beam velocity determined from the blind welds could not be applied directly to the line-type welding figures. Such low welding velocities led to poor surface finish producing large protrusions and intrusions. The reason for this lies in the proximity of neighbouring welding lines resulting in an already heated sample upon beam impact. The read rate (or frequency) was therefore increased to produce beam velocities of 200 to 400 mm/s. As the point density along one welding line was 50 pts/mm for most experiments the read rate was adjusted accordingly to 10000 - 20000 Hz.

A joint was reached only for currents greater than or equal to 2 mA. Only for very thin Mg-plates (0.25 mm) a current of 1.5 mA was sufficient. Large currents resulted in the liquefaction of magnesium during the entire welding time (for currents of 3 mA and above, depending on the Mg-plate thickness). A poor surface finish and a redistribution of the magnesium volume was the result. Therefore, the current was fixed to 2 mA for all subsequent experiments.

The spacing between the lines in the beam figures was varied from 1 mm to 0.25 mm. Individual lines are produced for a spacing of 1 mm. For 0.5 mm

the weld beads overlap on the surface as well as in most of the magnesium volume. There may, however, be small volumes in between the lines that were not affected directly by the beam. The sequence of the figure formation affects the size of these volumes through the previously induced heat: The first lines had a larger non-melted area in between than the lines later in the welding process because at this stage, the sample was already at a higher temperature. For a line spacing of 0.25 mm magnesium was directly affected by the beam in the whole volume underneath the 10x10 mm² beam figure.

(a)   (b)
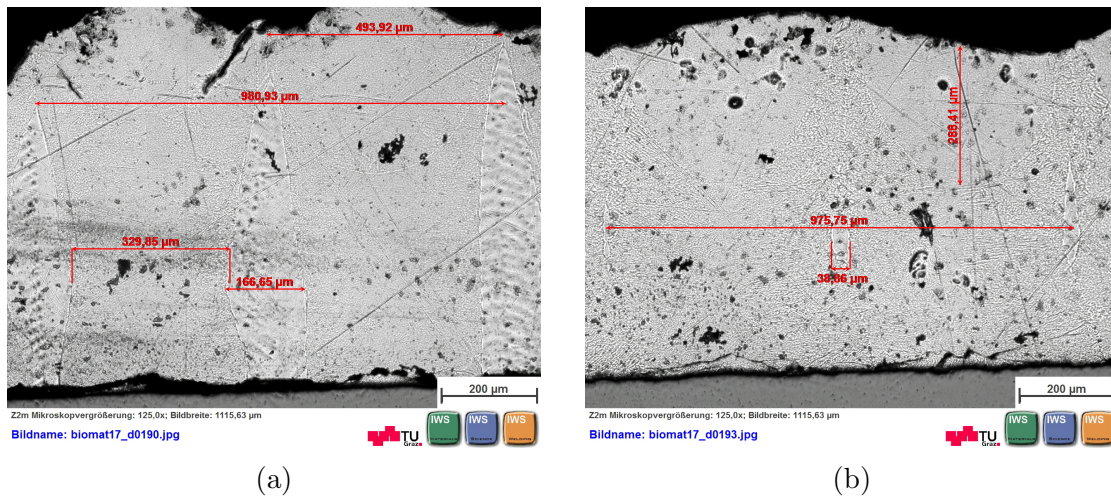
Figure 19: Non-molten areas in Mg2Ag between the beams for a line spacing of 0.5 mm (LOM image, I = 2 mA, frequency = 10000 Hz, pre- and postheated with 1 mA): (a) first beams of the beam figure; (b) last beams of the beam figure.

Multiple swipes of the same beam figure resulted in redistribution of the magnesium exposing the underlying titanium. Higher frequencies and appropriate waiting times in between the welding cycles may prevent this issue. Since already one swipe with appropriate parameters produced good results the realization of multiple swipes was not further investigated.

If the beam figure consists of random points on a 10x10 mm² large area, the energy input into the sample needed to be much higher than for the line-type deviation figure. It brought as a consequence that two successively targeted points were not adjacent physically anymore. This allowed the heat to be dissipated and the

magnesium to cool down locally until the next point was hit in its surrounding. Therefore, the frequency needs to be reduced and the welding time to be increased in order to get a good joining.

(a)   (b)
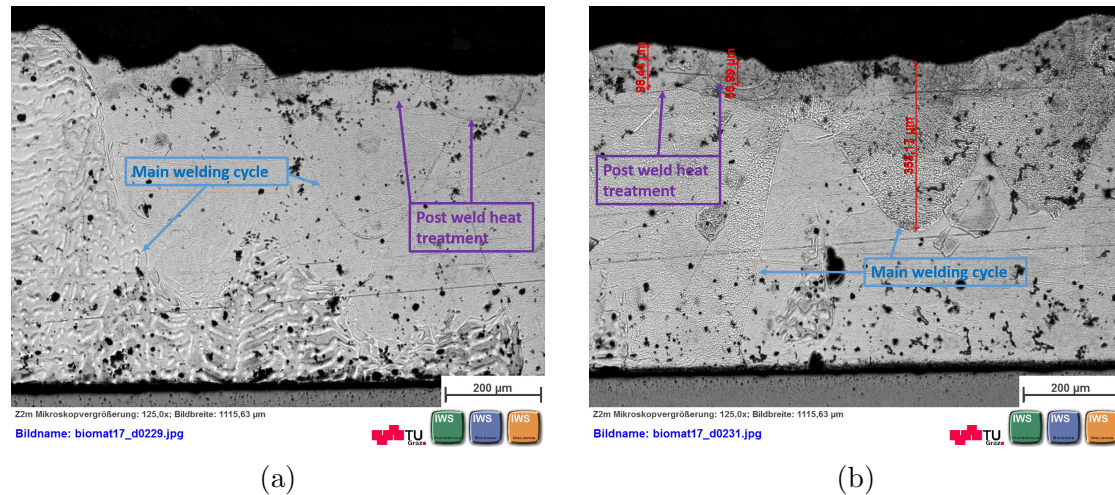
Figure 20: Penetration depth of single welding points in Mg2Ag for a random point beam figure (LOM image, I = 2 mA, frequency = 2000 Hz, pre- and postheated with 1 mA and 5000 Hz): (a) on the edge of the beam figure; (b) in the centre of the beam figure.

In table 8 the parameters are listed with their value range for which the best results were obtained for both line-type and random points beam figure. If the thickness of the magnesium plate is changed, the optimized parameters need to be adapted as well. In general the energy input per volume should remain similar for an optimal outcome, i.e. for thinner magnesium plates either a lower beam current, a higher frequency or shorter welding times need to be chosen.

4.3.3 Influence of energy input

In order to quantify the energy input into the sample, the energy of the whole welding process was calculated. The reference volume was considered to be the 10x10 mm^2 surface with the thickness of the magnesium plate as the third dimensional parameter. The thickness of the titanium plate was not included. Even though the energy of the electrons is transferred partly to the titanium the ma-

Table 8: Optimized parameters for electron beam welding for a Mg-plate with a
thickness of 0.8 mm

Parameter	value or range	
	lines	**random points**
constant parameters		
voltage	150 kV	
point density	50 pts/mm	-
modified parameters		
current	2 mA	
line spacing	0.25 mm (total overlap)	-
energy input	4 - 8 J/mm^3	20-25 J/mm^3
beam velocity	200 - 400 mm/s	-
frequency	10000 - 20000 Hz	2000 Hz
welding time	0.5 - 2 s	5 s

jority is released in the magnesium part and only later dissipated to the titanium.
Many effects need to be taken into account when calculating the energy input into
the two parts of the system: heat conduction within and between magnesium and
titanium, the heat capacity of the respective metal and heat radiation into the
surroundings. Heat exchange into the surroundings by convection does not take
place, because of the vacuum environment, however, the heat convection through
movement of the molten magnesium has to be considered. All energy input values
are therefore only considered to be comparative between the different experimental
parameters used.

In the case of a preheating or postheating cycle, additional energy was initially
introduced into the magnesium. However, this energy input was partly dissipated
during the waiting times either by conduction to the titanium part or emitted by
radiation to the surroundings.

The energy input per unit volume is thus defined as:

$$E_{input} \; \left[\frac{J}{mm^3}\right] = \frac{voltage \; [V] * current \; [A] * welding \; time \; [s]}{beam \; deflection \; area \; [mm^2] * Mg - thickness \; [mm]} \quad (3)$$

The content of titanium inclusions correlates with the energy input. The higher
the energy input, the more amount of titanium inclusions are present in magne-
sium (figure 16). As the energy input was decreased to remove welding defects,

also the amount of titanium within magnesium was reduced. This will have a positive impact on biocompatibility: If the material is employed as an implant and magnesium dissolves gradually over time, titanium inclusions will be released into the body environment. High concentrations of titanium particles were shown to induce an inflammatory response and may compromise cell viability [57] or result in bone loss [58] and eventually result in implant instability and failure.

In respect to the presence of porosity, both macro- and microporosity appeared in magnesium after electron beam welding. Microporosity was already present in the as cast pure magnesium. The welding process introduced, however, additional pores: Figure 21 shows microporosity of magnesium outside the welding volume and the welding areas for samples carried out with different parameters.
The porosity content was evaluated using ImageJ, an image processing and analysis program [59]. The percentage of the porosity was evaluated and compared with the energy input per volume. The data is fitted with a polynomial trend line of second degree which matches very well to the experimental values (see figure 21e). Therefore, by reducing the energy input microporosity can be reduced as well. However, these results can merely be considered as a trend as only a small sampling was analysed.

(a)

(b)

(c)

(d)

(e)
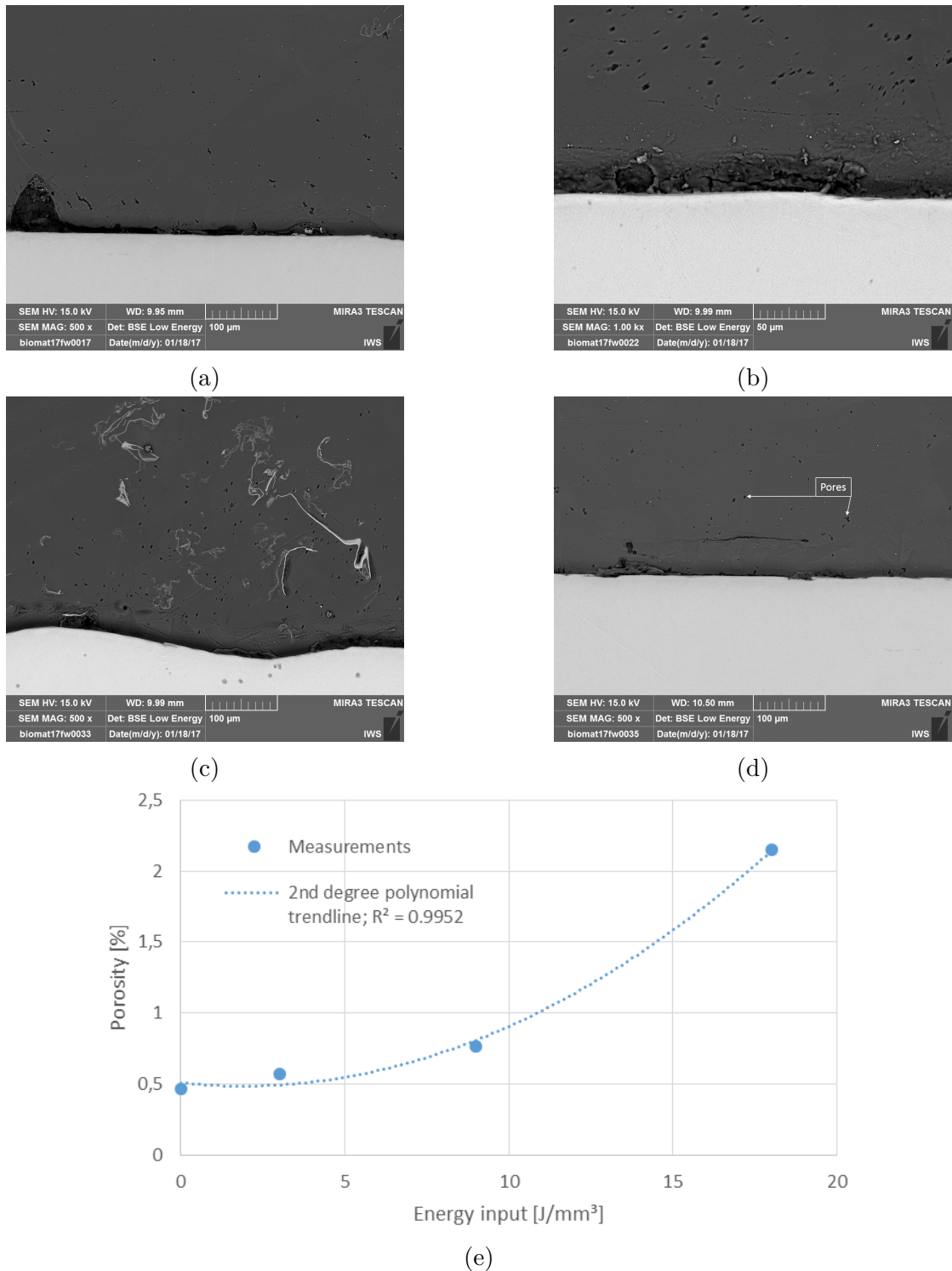
Figure 21: Dependence of microporosity on energy input: (a) sample without treatment; and for energy inputs of: (b) 18 J/mm³, (c) 9 J/mm³, (d) 3 J/mm³; (e) microporosity percentage vs. volumetric energy input.

4.3.4 Influence of preheating and post weld heat treatment

Macroporosity is present in the bulk as well as at the Mg-Ti interface. These pores are potential nucleation sites for cracks and are particularly harmful if present at the interface where there is a risk of detachment. Microscopic analysis showed that macroporosity is often present directly below the first welding line of the beam figure (see figure 22a). This is due to the abrupt heat input into the cold sample. The steep temperature gradient between the initial beam impact zone and the rest of the sample causes differential thermal expansion and is the source of this porosity. Macroporosity can be prevented by preheating the sample. The temperature of the volume surrounding the beam impact is now elevated prior to welding and the sudden heat input into the sample is alleviated. In order to produce a uniform heating the beam figure is traced at a lower current of 1 mA before the actual welding process. Indeed, macroporosity can be reduced significantly as is shown in figure 22b. Both specimens are welded with the same parameters except that one is pre- and postheated. This effect is mainly attributed to preheating, as the macropores originate in the actual welding process and a postweld heat treatment delivers too little energy to actually dissolve these large porosities.
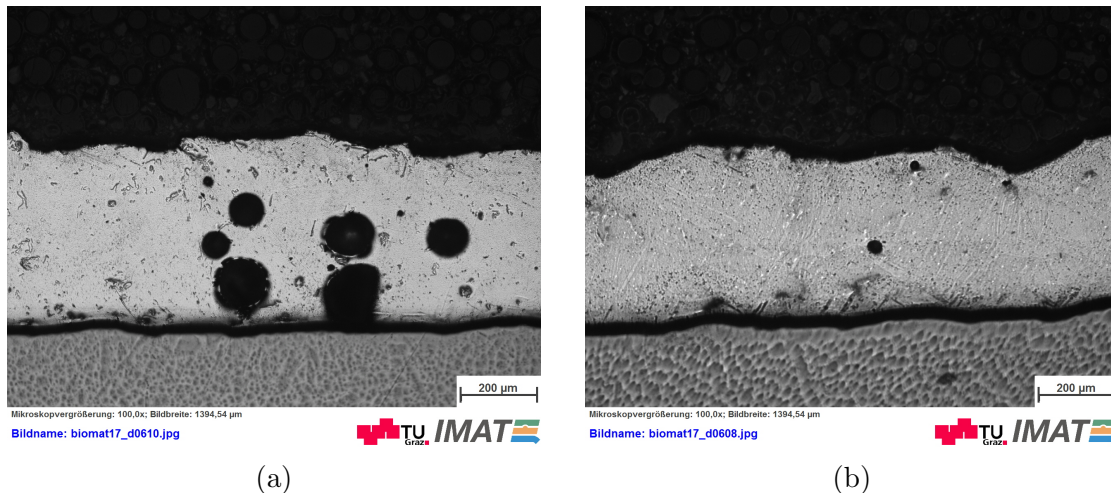
Figure 22: Influence of preheating on macroporosity (frequency = 10000 Hz, line spacing = 0.5 mm): (a) non-preheated sample; (b) preheated sample with 1 mA.

In addition to pores, cracks were also formed during the welding process. These were predominantly observed in the Mg-Ag alloy but also in pure magnesium fast cooling gave rise to some smaller cracks, mostly a few tens of micrometres above the Mg-Ti interface. Both preheating and post-weld heat treatments reduced the occurrence of cracks. Preheating relieves internal stresses. A post-weld heat treatment reduces the cooling rate and removes residual stresses before the sample has cooled to prevent brittle fracture provoked by negative thermal expansion, especially the difference in contraction between titanium and magnesium. Therefore, the waiting time between welding and post-weld heat treatment needs to be chosen diligently. A waiting time of 2 seconds produced satisfactory results: The extent of cracks in Mg2Ag was reduced significantly while cracking in pure magnesium was removed completely.

The fact that cracks do not form directly at the interface, but rather at some distance in the magnesium suggests a substantial joining strength between the two metals. A similar result was found for fracture tests of an ultrasonic spot welded Mg-Ti joint by Ren et.al. where the fracture initiated inside the magnesium alloy rather than at the welding interface [50].

(a)   (b)
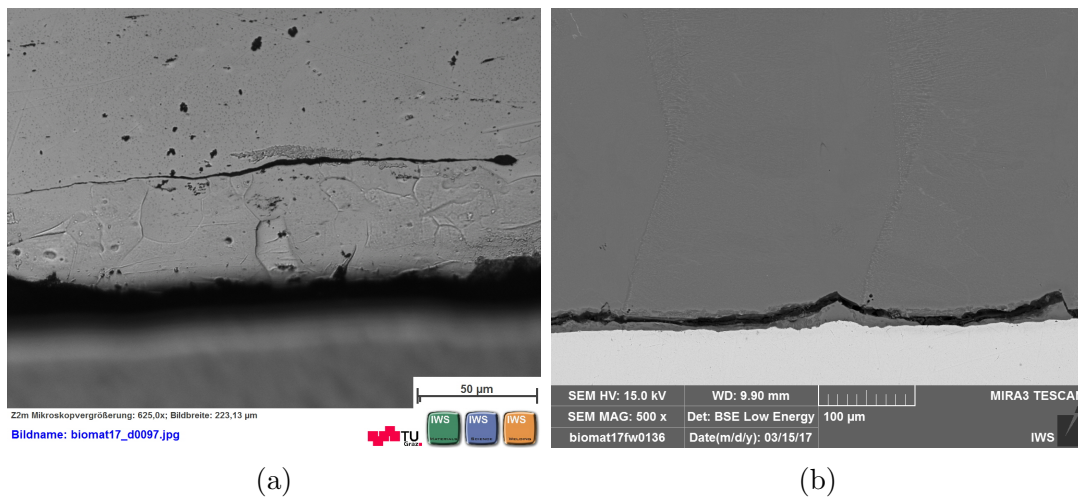
Figure 23: Cracking at and above the interface (without preheating or post-weld heat treatment): (a) small crack for pure Mg (LOM image); (b) severe crack for Mg2Ag (SEM image).

The penetration depth of preheating and postheating cycles was only about 250 µm and the molten zone did therefore not reach the titanium-magnesium interface. This was a result of a lower welding (1 mA) current and higher frequency (20000 Hz). Nevertheless the provided heat input and subsequent transfer proved to be sufficient for a substantial improvement of the welding outcome.

The analysis of samples produced with the same welding parameters showed high repeatability: The obtained macroscopic and microscopic properties like interface quality, porosity, crack behaviour, surface finish and microstructure were very similar.

4.4 Microstructural changes after EBW

4.4.1 Pure Magnesium

The type of beam figure affected the grains size of magnesium: For a random points beam figure many small grains are produced throughout the magnesium and in particular close to the surface, where the sample is hit and melted several times.

For a line-type beam figure after electron beam welding small grains appear in the centre of the weld like in the case of the blind weld. Some samples exhibit no such grains, but the large original grains are cut instead in the centre of the weld bead. Furthermore, small grains are produced both on the magnesium surface and at the Mg-Ti interface where grain growth is inhibited due to rapid solidification.

Figure 24: LOM image of the microstructure of pure magnesium after EBW with a random point beam figure

(a)

(b)

(c)

(d)

Figure 25: LOM images of pure magnesium after EBW with a line-type beam figure: (a) elongated grains and (b) small grains in the centre of weld bead; (c) grains cut by the beam at the centre of the weld bead; (d) small grains at the interface between magnesium and titanium.

4.4.2 Mg2Ag

The grain size of electron beam welded Mg2Ag was determined to 150 µm. Welding affects also the dendritic structure of the Mg2Ag alloy: Figure 26a shows finer dendrites compared to the unwelded sample (figure 11). Furthermore, the distribution of silver within the alloy is changed, being concentrated between the finer dendritic arms. Observations in the scanning electron microscope show the elemental distribution within the alloy. Brighter areas in the back-scattered electron signal arise from the presence of an element with a larger atomic number, i.e. silver. A larger portion of brighter areas is visible in the zone at the onset of a new beam and on the convex side. In figure 26b the border between two welds is depicted. On the left side the enriched areas are much smaller but distributed more uniformly. Right of the border, aside from the titanium inclusion in the centre, silver is enriched between dendrites and at grain boundaries. The volume to the right was melted twice during the welding process. This leaves more time at an elevated temperature for silver atoms to diffuse and to accumulate in certain areas. Nevertheless the available time was too short for them to form proper precipitates: The enrichment-areas had blurred edges which indicates that no equilibrium precipitates have been formed, but rather just a silver-enriched transition lattice.

In figure 27 different microstructures of the Mg2Ag alloy are observed: This sample was not preheated. Therefore in the centre of the picture there was a remnant of unwelded area. The dendritic structure contains silver-enriched areas between the dendrite arms, with some more developed precipitates. The first beams of the welding beam figure are visible on the right hand side. These beams did not reach the interface due to the beam hitting a cold sample. As a result also the cooling rate was faster and there was no time for silver to diffuse and is therefore present in supersaturated solid solution. The weld bead on the left hand is the last welding line in the beam figure. When the electron beam welded this area, the sample as a whole was a lot warmer compared to the first welding lines. Therefore, the weld bead was not only broader but also the temperature elevated during and especially after the passing of the electron beam. Cooling happened slower and thus silver could diffuse more easily. However, diffusion paths were rather small and the
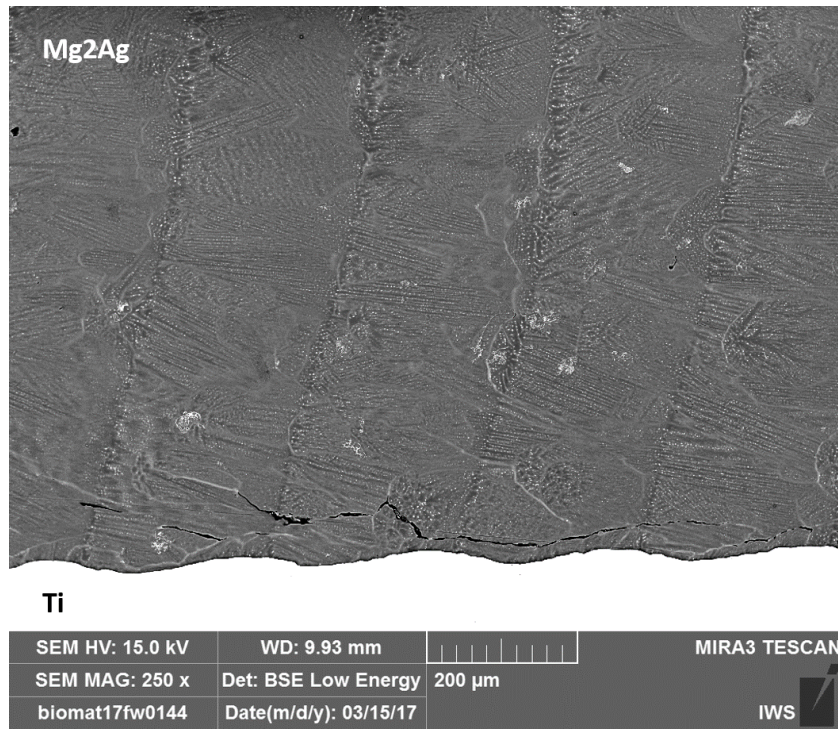
(a)
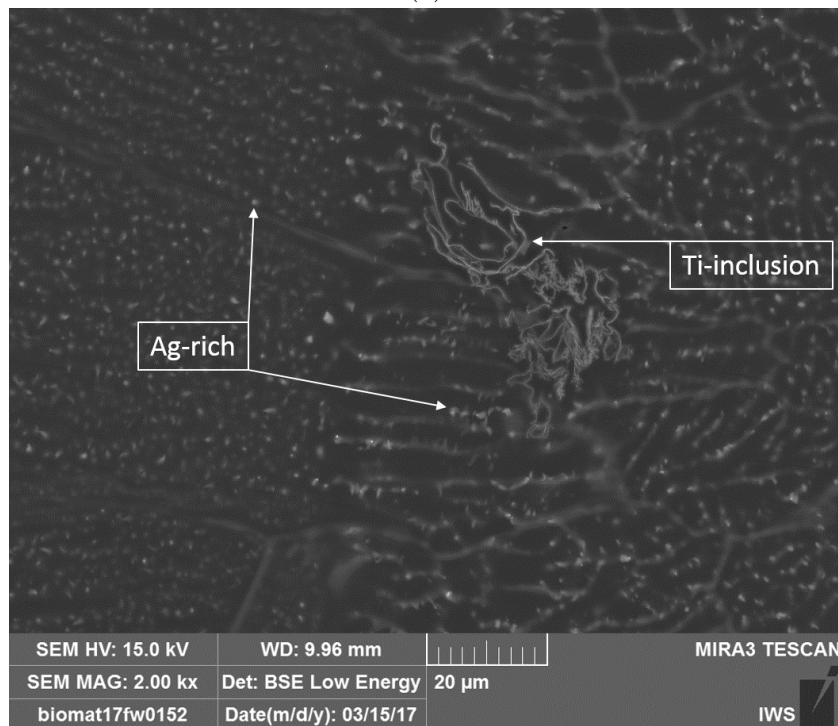
(b)

Figure 26: SEM image of a dendritic structure of electron beam welded Mg2Ag: (a) overview and (b) detailed view of the border of a welding beam.

49

silver-enriched areas and precipitates were finely dispersed. Also some macroseg-
regation was noticeable: The border between the last beam and the unwelded area
is clearly enriched in silver. Macrosegregation is, as well, a consequence of the
lower solubility of silver in solid magnesium compared to liquid magnesium.
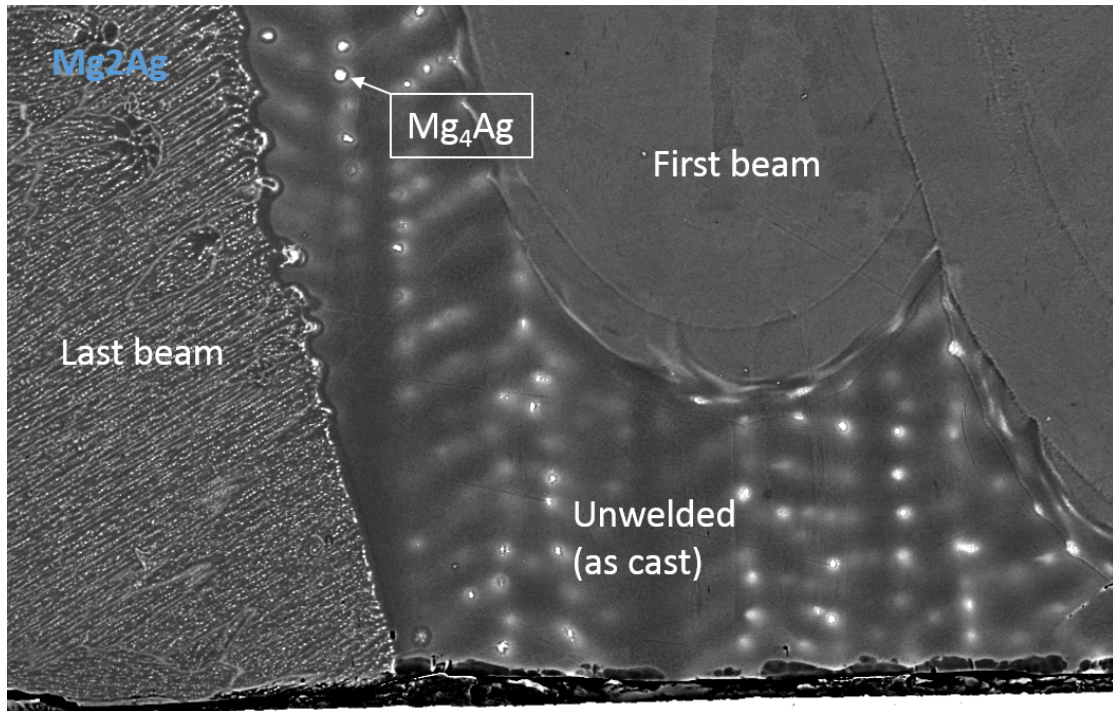
Figure 27: SEM image (BSE mode) of the first and last welding lines in a Mg2Ag
          sample

4.4.3 Titanium

During the welding process also the titanium microstructure was altered due to
the impact of the beam on titanium and subsequent rapid cooling: Titanium
martensite was formed, because the time for diffusion was too short, resulting in

an acicular structure transformation [55]. The higher the energy input, the deeper the martensite extents into the bulk. In this work, martensite was observed up to 150 µm from the interface. Figure 28 shows the grain structure with the equiaxed grains of the base material on the bottom and the martensite near the Mg-Ti interface.
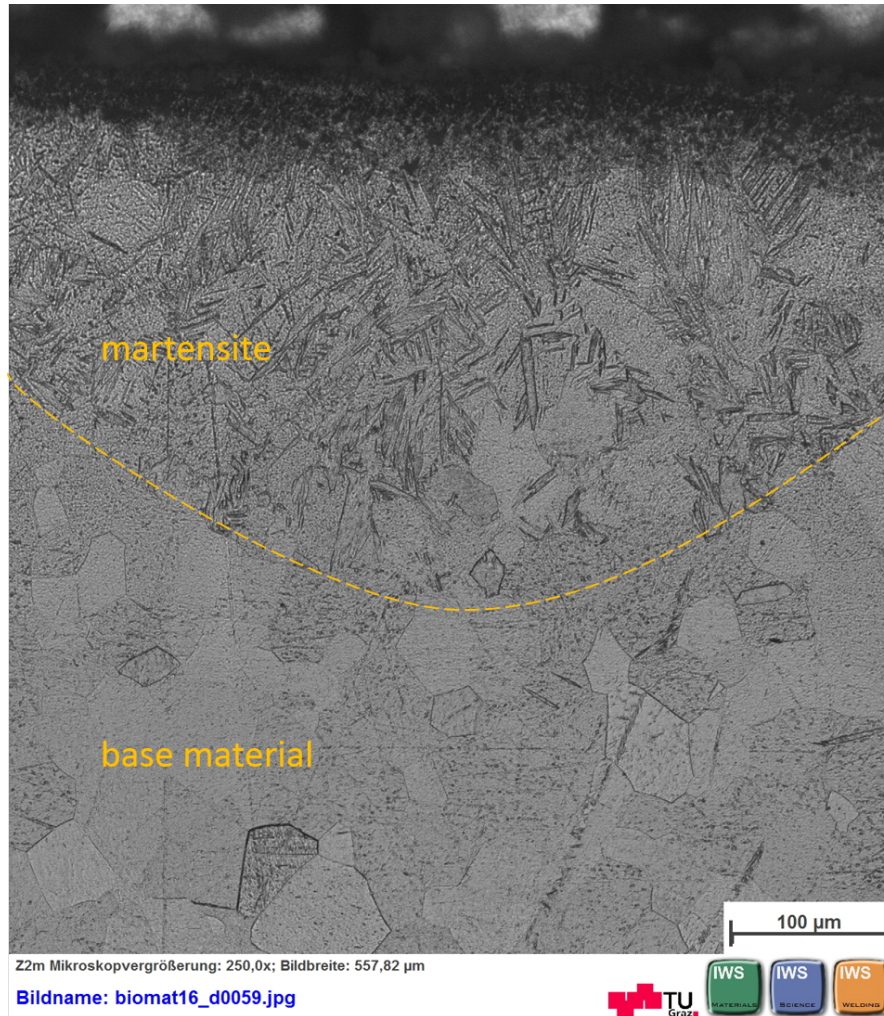
Figure 28: Titanium microstructure after EBW: martensitic transformation (LOM image, etched with hydrofluoric acid)

4.5 Interface characterization

Interface characterization was difficult to carry out as a consequence of the step-like configuration due to the difference in polishing rate between magnesium and titanium. Figure 29) shows the interface between commercial magnesium and titanium. There was joining along the whole interface. However, the interface was not flat, but showed topographical regularities which correspond to the line spacing used for the respective sample as can be seen in figure 26a. Also on a smaller scale some rugosity are visible (see figure 29).
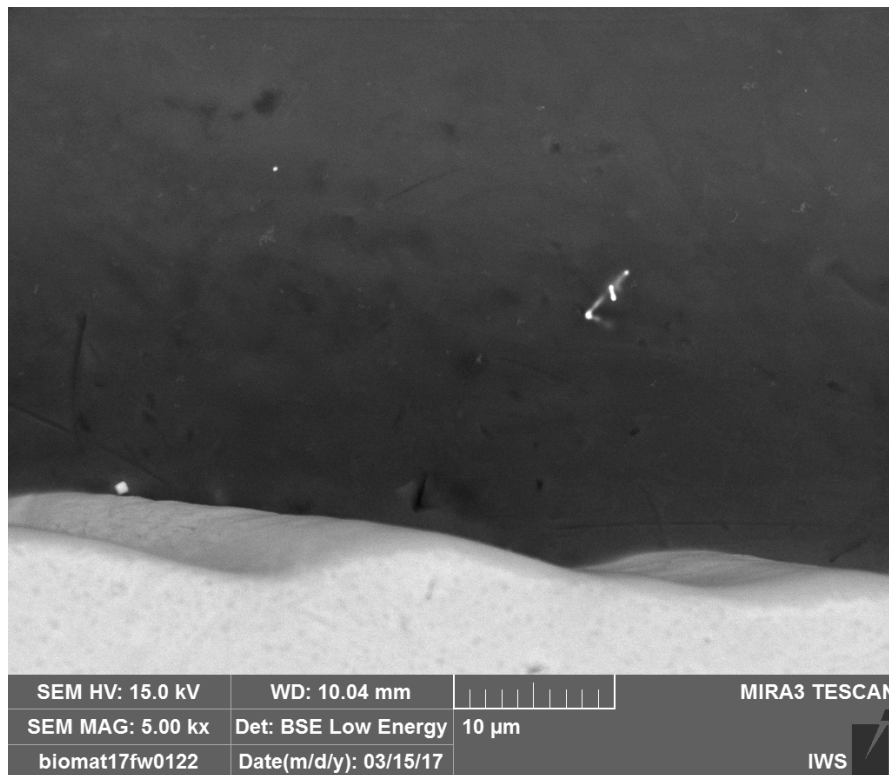
Figure 29: SEM image (BSE mode) of the interface between magnesium (top) and titanium (bottom)

EDX line scans were carried out to study the element distribution at the interface. The results for Mg-Ti and Mg2Ag-Ti are depicted in figure 31 and 32 respectively. The concentration of magnesium drops at the interface while the titanium content increases. Directly at the interface, magnesium and titanium content are the same. At the Mg2Ag-Ti interface silver concentration drops basically to zero: There is

no indication of diffusion of silver atoms into titanium, even though the solubility in titanium is significantly higher for silver than for magnesium.
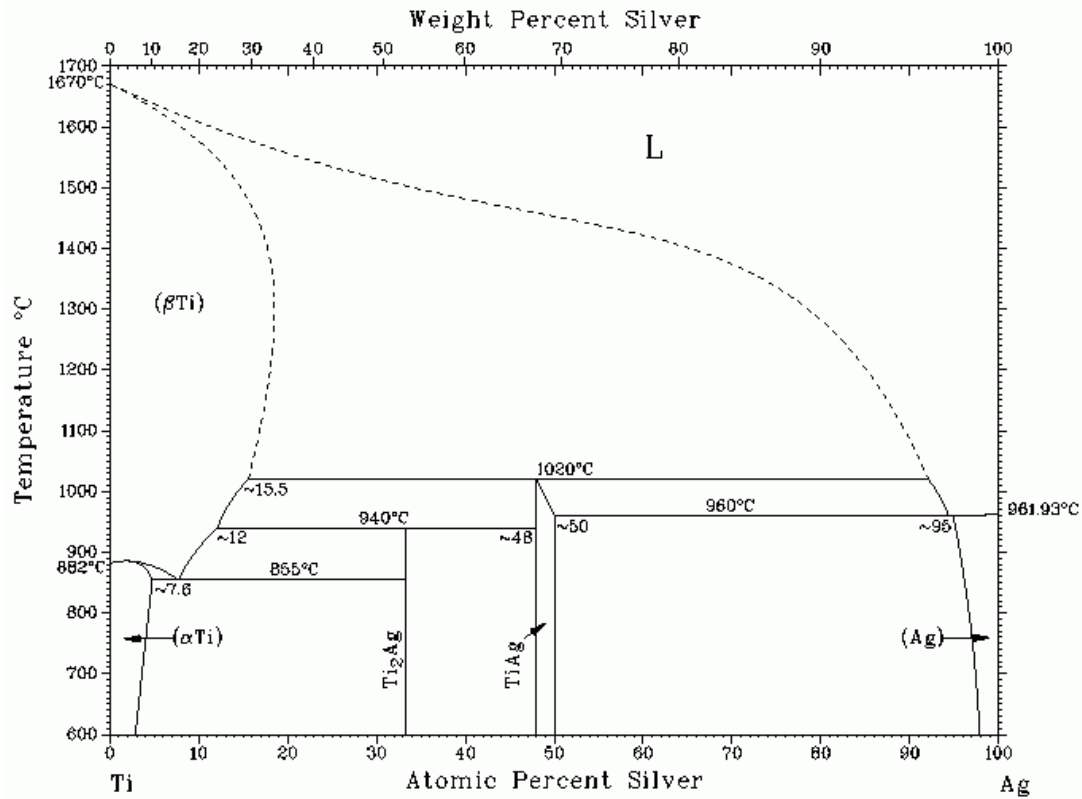
Figure 30: Ag-Ti phase diagram [39]

The problem with EDX measurements are the quite large interaction volumes of x-rays. The detected x-rays from a point measurement derive from a volume in the order of micrometres. The exact spatial resolution depends on the atomic number of the sample and the accelerating voltage. Therefore magnesium concentration within titanium or vice versa cannot be totally attributed to interdiffusion. A high count rate of magnesium in titanium close to the interface may just be the consequence of an excitation of an x-ray (with a characteristic wavelength) in the nearby magnesium lattice. Also, mutual penetration depth approaches zero no later than 2 µm from the interface.
An indication that there may be some at least some diffusion of titanium into mag-

nesium is the fact that at some titanium was melted during welding as indicated in the presence of titanium inclusions in magnesium. However, the extent of this interdiffusion between the two metals needs to be further studied. TEM measurements should be carried out to investigate element distribution at the interface. Nevertheless, magnesium and titanium were bonded along the whole interface and the bond seems to be quite strong. A possible explanation for this behaviour may be a firm anchoring which takes place upon solidification of molten magnesium on the titanium surface.
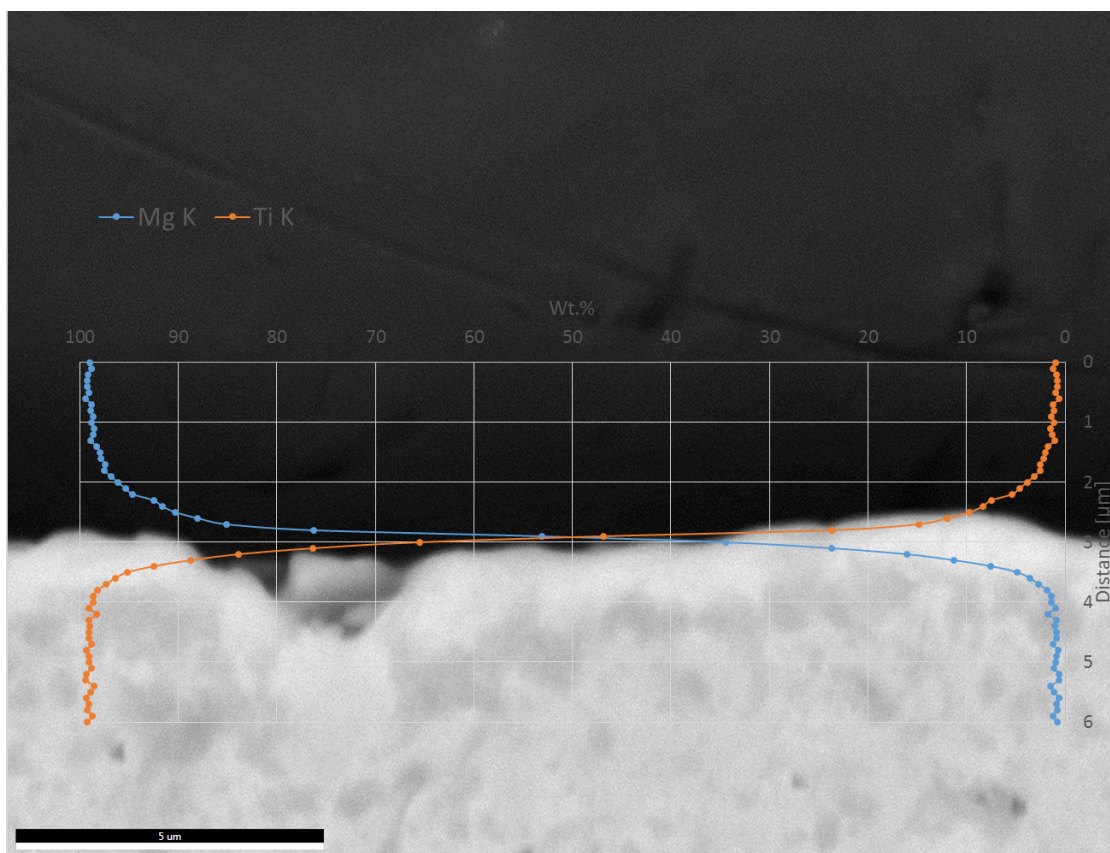
Figure 31: Mg-Ti interface with element composition (wt.%) perpendicular to the interface
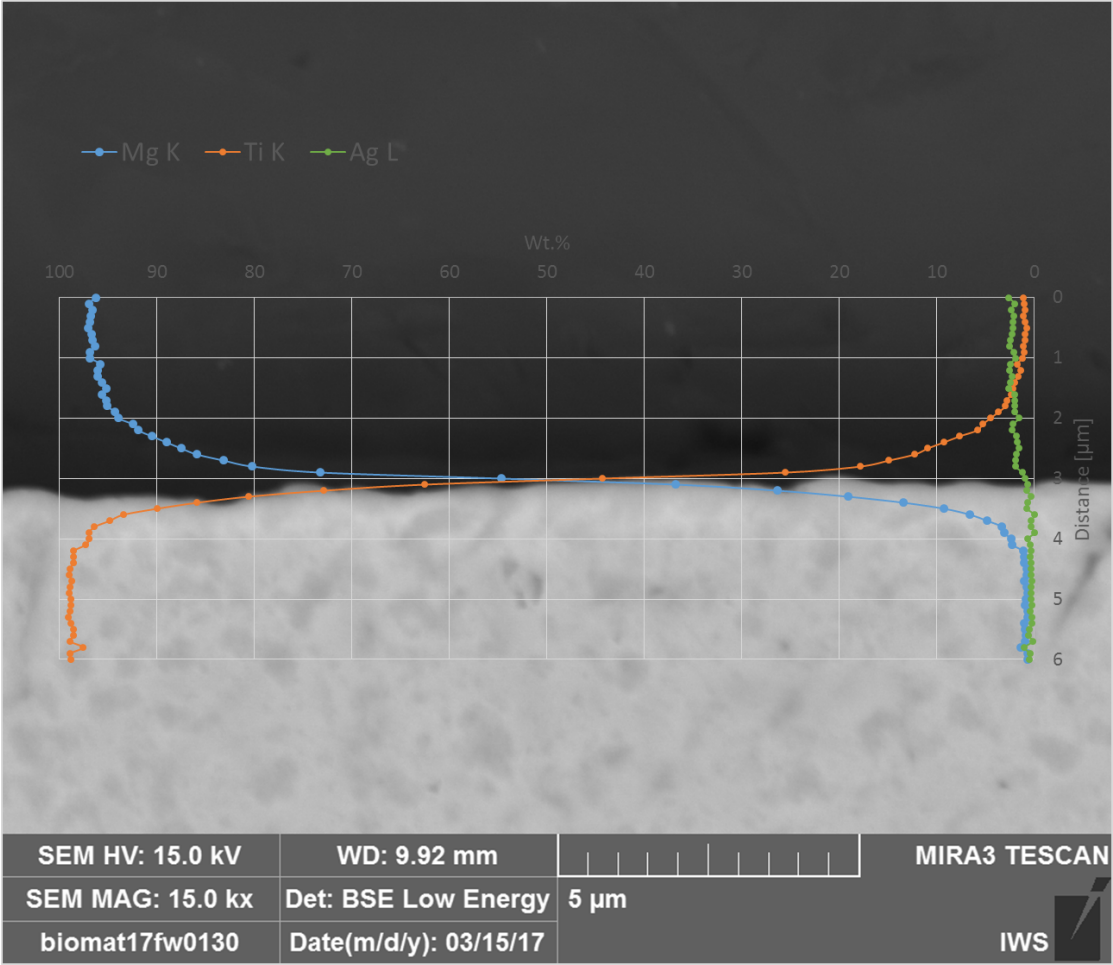
Figure 32: Mg2Ag-Ti interface with element composition (wt.%) perpendicular to the interface

4.6 Heat treatments

Solution treatments at 450°C and 24 hours and subsequent quenching resulted in cracks, partial detachment of titanium and the magnesium alloy and severe oxidation of titanium. Figure 33a shows the characteristic blue coloration of titanium oxide (TiO_2) which forms on titanium surface as it is exposed to air atmosphere at high temperature. Also the magnesium surface is heavily oxidized.

The fracture surface is depicted in figure 33b. Once again, fracture does not occur at the interface but some magnesium adheres to the titanium surface. The distortions and subsequent detachment of magnesium can largely be attributed to the volumetric changes caused by quenching as there is a large difference in the coefficient of thermal expansion between titanium and magnesium (compare tables 1 and 3).

(a)   (b)
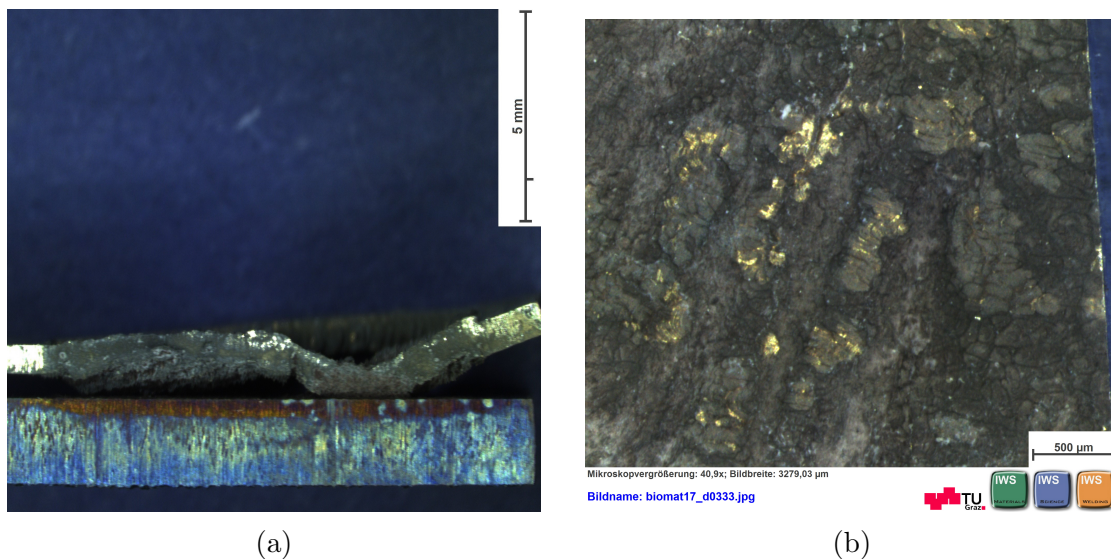
Figure 33: Mg2Ag and titanium solution heat treated at 450°C for 24 hours (a) titanium covered with TiO_2 and detachment between Ti and Mg2Ag; (b) fracture surface: Mg2Ag adheres to titanium.

Samples after solution treatment during 2 hours showed also oxidation and cracks along the interface, but less severe, with large portions of the interface staying bonded. Furthermore, cracks perpendicular to the Mg-Ti interface appeared as a result of thermally induced stresses.

(a)   (b)
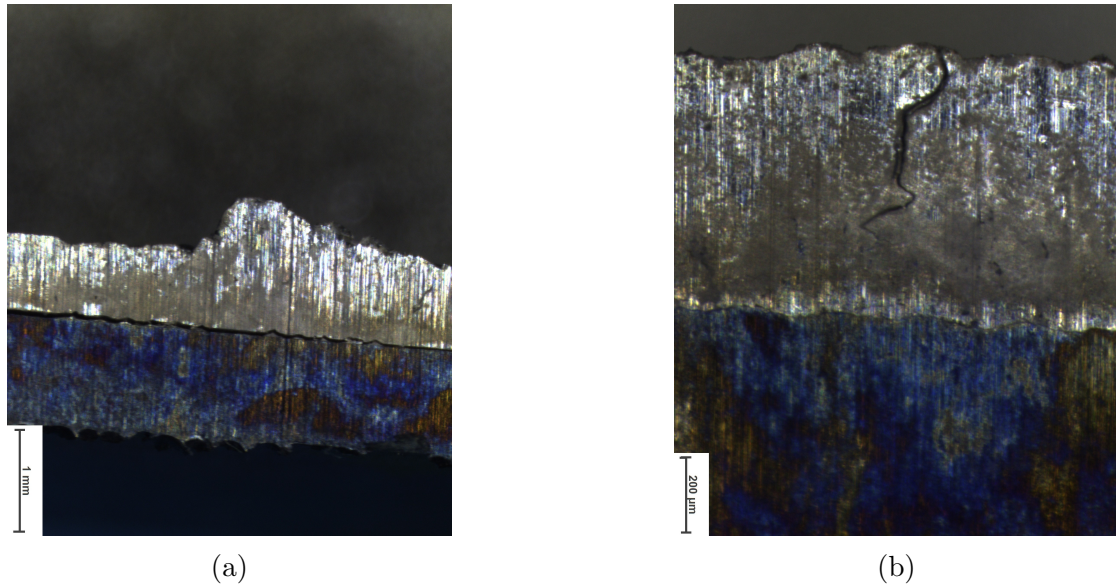
Figure 34: Mg2Ag and titanium solution heat treated at 450℃ for 2 hours: tita-
nium covered with TiO$_2$, (a) crack at the Ti-Mg2Ag interface, (b) crack
in Mg2Ag perpendicular to the interface, but bonded interface.

For the ageing treatments neither cracks nor debonding was observed. Figure 35
shows a Mg2Ag sample which was heat treated at 180℃ for 1 hour. Some small
precipitates were visible at the grain boundaries where it is easier for silver atoms
to diffuse. These precipitates were about 200 nm in diameter. During ageing at
180℃ and 24 hours resulted in precipitates of up to 850 nm in diameter, while for a
higher temperature of 220℃ larger particles precipitated at the grain boundaries.
Moreover, precipitates, although smaller and less frequent, were also found in the
bulk. The volume molten two times during welding were higher in precipitate
concentration. In all aged samples, silver enriched areas were present, without
formation of precipitation.

The precipitates were analysed with EDX-measurements and showed a larger con-
centration of silver atoms compared to the bulk as is shown in figure 37 for a point
measurement at various sites within the alloy. However, due to the small size of the
precipitates the composition of the intermetallic phase could not be determined
by EDX. The interaction volume for x-rays is much larger than the size of the
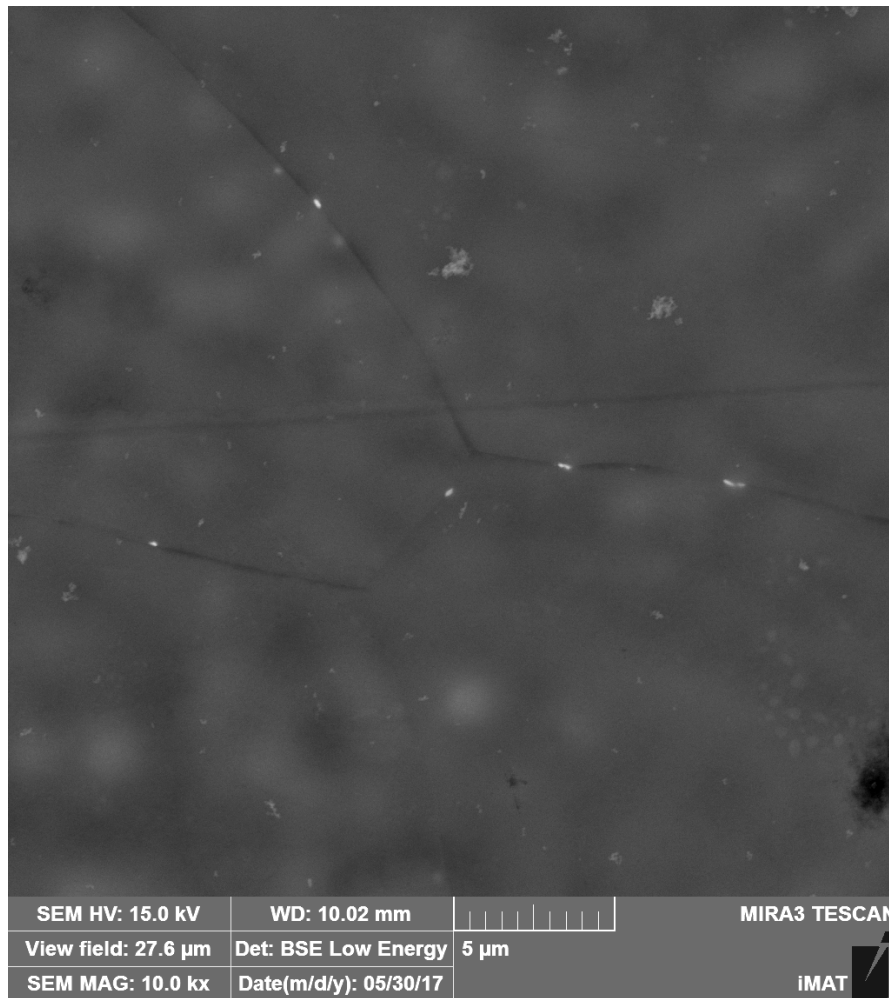
Figure 35: Precipitates at the grain boundaries of an aged Mg2Ag sample at 180°C for 1 hour

precipitates. From literature and the phase diagram (figure 4) the second phase can be deducted to be Mg_4Ag [56]. Studies suggest a reduction of the corrosion rate due to the present of the second phase [31].
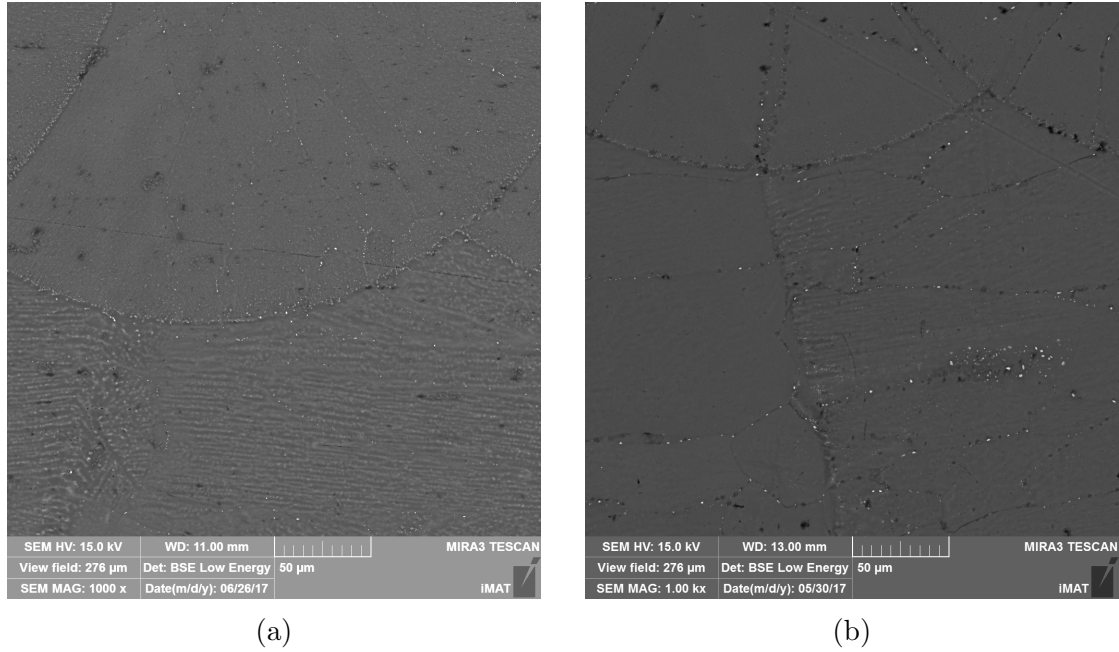
Figure 36: SEM image of aged Mg2Ag after electron beam welding: (a) 180°C for 24 hours; (b) 220°C for 24 hours.
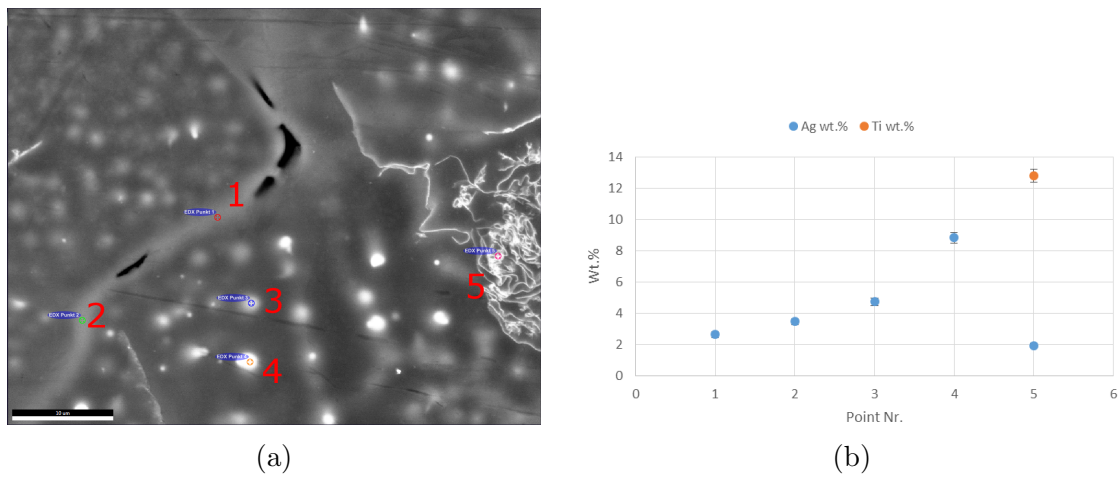
Figure 37: EDX point analysis of a Mg2Ag alloy with silver enriched areas and precipitates: (a) location of measurement points; (b) element concentration for each measurement point.

4.7 Hardness evaluation

The hardness measurements of pure magnesium, Mg2Ag as cast and Mg2Ag after electron beam welding are given in table 9. Hardness measurements in magnesium and alloys proved to be difficult: Many indents were misshapen and did not satisfy measurement standards and had to be rejected. This behaviour was less severe for aged samples.

Pure magnesium had a very low hardness: Magnesium is a very soft material and

Table 9: Vickers hardness for a force of 100 ponds (HV 0.1), a slope of 2 ponds/s and a holding time of 15 seconds

Material	HV 0.1
pure Mg	29 ±2
Mg2Ag (as cast)	39 ±2
Mg2Ag (after EBW)	45 ±2
Ti Grade 2	155 ±4
Ti Grade 2 (martensite)	213 ±8

the large grains contributed to its low hardness. Hardness of Mg2Ag was higher compared to the unalloyed metal. The atomic radius of silver is 11% larger than that of magnesium, which results in a strong solid solution effect [56]. Furthermore, the addition of silver may produce a grain refining effect: The smaller grains size lead to an increase of hardness [31].

The difference in hardness between the as cast magnesium alloy and the sample after electron beam welding was due to the finer dendritic structure and the associated increase in phase boundaries. Moreover, silver was more evenly distributed within the magnesium volume because of the finer dendrites.

Figure 39 shows the hardness measurements for Mg2Ag as cast, after welding and of the heat treated samples. Hardness values are basically constant over the whole ageing range. Error bars represent the standard deviation of the respective measurement series. Hardness measurements show thus a large divergence.

The reason for this behaviour can be attributed to the strong solid solution effect of silver in magnesium. By diffusion of silver atoms the strong solid solution effect was attenuated while precipitation hardening takes place. These two effects seem to have a similar impact on hardness. As described in section 4.6 the longer the

(a)   (b)
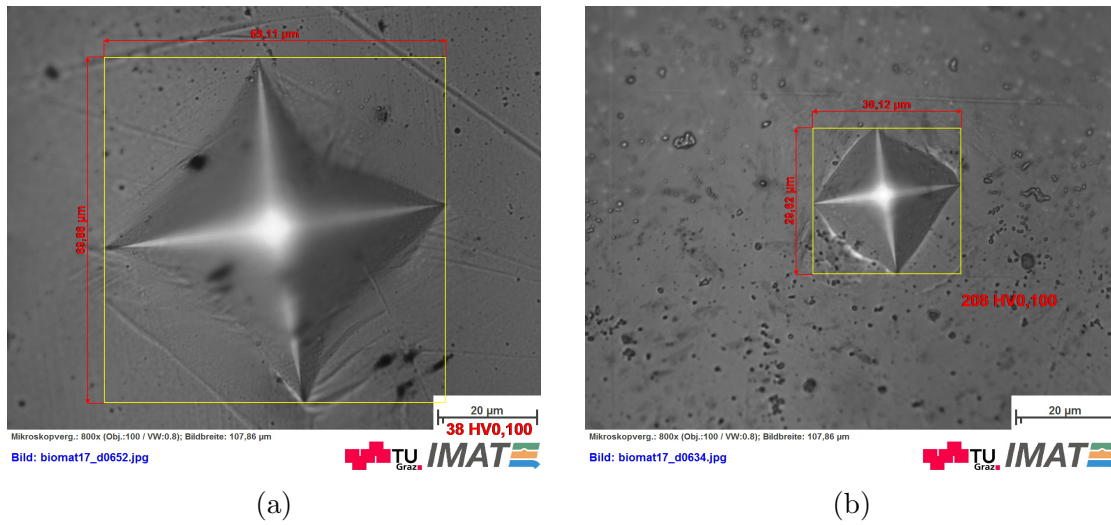
Figure 38: Indents for Vickers hardness HV 0.1: (a) Mg2Ag as cast; (c) titanium
martensite.
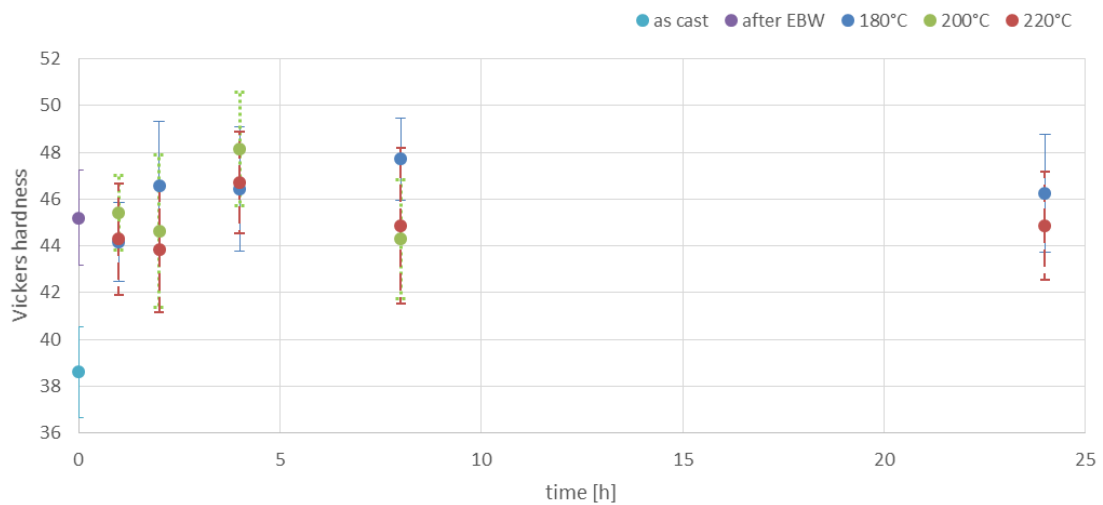
Figure 39: Vickers hardness HV 0.1 for Mg2Ag as cast, after EBW and for various
ageing temperatures and times

diffusion time, the larger the precipitates become, especially at grain boundaries.
Simultaneously the silver concentration was reduced elsewhere. Instead of small,
uniformly distributed, silver-enriched volumes, silver was now present in precipi-
tates, while the surrounding area is deprived of it (see figure 36). The increment of
hardness due to welding of cast Mg2Ag was also an indicator that smaller Mg_4Ag

precipitates and/or silver-enriched areas were more favourable to higher hardness than a few large ones.

The border between two beams was measured with low force in order to obtain small enough indents to find differences in hardness on dimensions this small. Hardness measurements from this series were not directly comparable with the ones performed with higher force. However, local hardness differences could be detected: Hardness was measured at the border between two beams, on the left of it and on the right of it as set out in figure 26b. The border of the beam (64 HV0.01) was found to be significantly harder than the surroundings. This is the consequence of macrosegregation, i.e. silver being transported to the border of the molten zone which therefore becomes enriched in silver and permits the formation of larger and more precipitates. Also, the area to the right (59 HV0.01) was harder compared to the area to the left (54 HV0.01) due to the distribution of precipitates as mentioned in section 4.4.2.

The hardness measurments suggest that with different treatments the mechanical properties can be slightly adjusted to specific needs. Finally, Vickers hardness of cortical bone was determined to be 49.8 [31] which compares quite well with the Mg2Ag alloy.

Titanium hardness was measured to be 155 ± 4 HV, while the martensite formed due rapid cooling after heat input of the electron beam was much harder: 213 ± 8 HV. After the dissolution of magnesium this martensitic hardening of the surface may improve wear resistance and prevent detachment of particles forming potentially harmful debris in body tissue.

4.8 Surface characterization

In figure 40 the magnesium surface after electron beam welding for a line-type beam figure and for a random points beam figure are depicted. In the detailed view solidification lines are visible: circular around the impact point and semi-circular along the welding lines. One single impact point is surrounded by several circular solidification lines and the impact points are larger in already heated areas as can be seen in figure 41b.
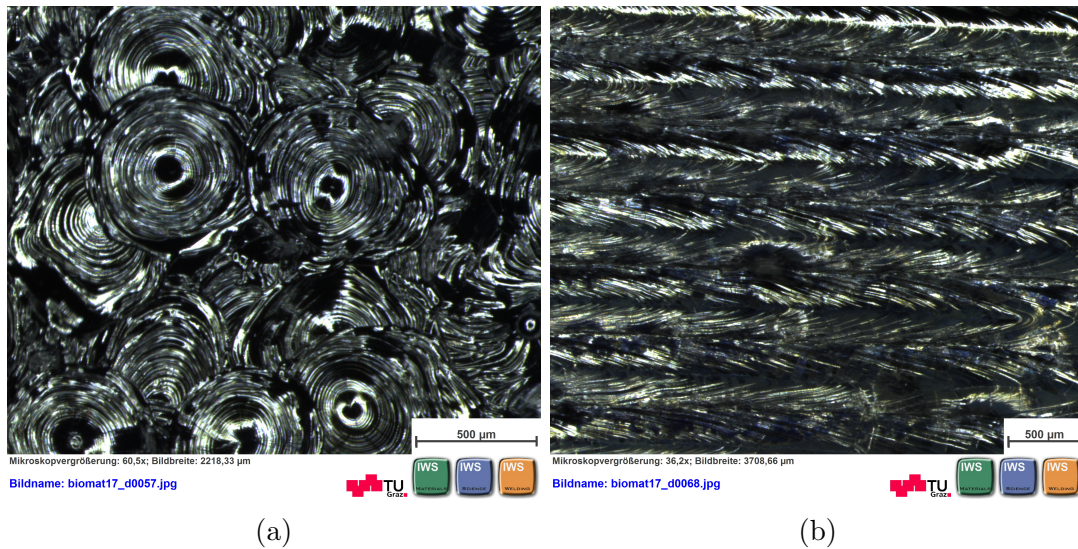
Figure 40: Details of magnesium surface for different beam figures: (a) random points; (b) line-type.

Large heat inputs were detrimental for all beam figures and resulted eventually in revealing the underlying titanium. For the line-type beam figure a too high energy input (above 8 J/mm^3) resulted in a redistribution of the molten magnesium by the electron beam exposing the subjacent titanium plate because the welding direction was the same for each welding line (compare figure 41a). This may be avoided by alternating the welding direction for each line. Similarly for the random points beam figure high energy input (be it high voltage, current or long welding times) heated magnesium excessively and did not only melt but evaporate it on a large scale producing a hole in the centre as seen in figure 41b.

Mikroskopvergrößerung: 12,6x; Bildbreite: 10,66 mm
Bildname: biomat17_d0166.jpg

Mikroskopvergrößerung: 17,2x; Bildbreite: 7,81 mm
Bildname: biomat17_d0059.jpg

(a)   (b)
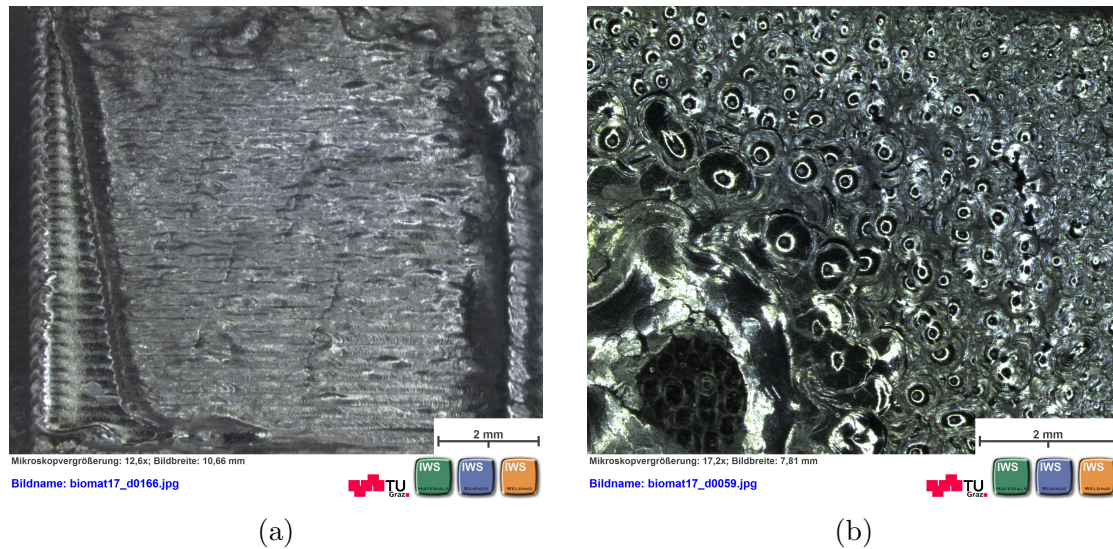
Figure 41: Detrimental effects of too high energy input: (a) material redistribution (energy input = 8 J/mm^3); (b) evaporation (Mg-plate thickness = 0.3 mm).

4.8.1 Topography

Figure 42: Alicona 3D surface picture of magnesium (line spacing = 0.25 mm, frequency = 10000 Hz)
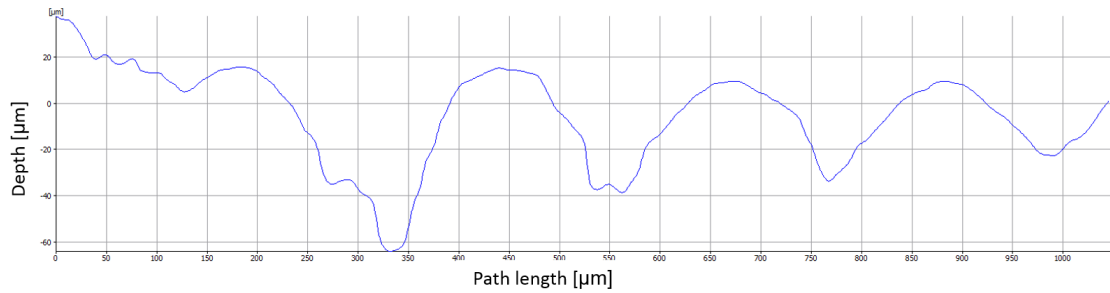
Figure 43: Primary profile of the magnesium surface perpendicular to the welding
          lines

The magnesium surface measured with Alicona is illustrated in figure 42. The
groove spacing depended on the distance of the welding lines. Also, solidification
lines were visible, although some oxidation of the surface was already present. The
roughness perpendicular to the welding lines is depicted in figure 43. The mean
height difference between peak and valley was determined to 47 µm but with a
large variance with values ranging from 19 µm up to 97 µm. The grooves and
ridges were not developed equally on the surface as can be seen in figure 44 where
a height profile is superimposed on the photo in the form of a colour scale. In
general a quite rough surface was formed with a large new surface created: The
increment of the surface was 21.2%. R_a and the R_q value were measured parallel to
the welding lines both on the top of ridge and halfway between ridge and groove.
The results are given in table 10. Roughness was larger halfway between ridge and
groove, while waviness was larger on the top. The discrepancy between R_a and R_q
value indicates that the surface was not uniformly rough but it contained larger
non-periodic irregularities as well.

The titanium surface after deep etching is displayed in figure 45. Surface irregulari-
ties were similar to magnesium: The distance between the welding lines determined
groove spacing and solidification lines were also present along the welding lines,
which can already be seen in figure 29. The distance between the solidification
lines was measured to 18 ±4 µm. The titanium surface was, however, less rough
than the magnesium surface. The increment of surface was determined to 3.2%,
much flatter than for magnesium. Also the profile depth was much lower with an
average of 11 µm.

Table 10: Roughness for magnesium and titanium surface after EBW

Parameter	Mg		Ti	
Roughness depth	47 µm		11 µm	
Increment of surface	1.212		1.032	
Roughness ridge	R_a = 465 nm R_q = 659 nm	$\frac{R_q}{R_a}$ = 1.42	R_a = 572 nm R_q = 757 nm	$\frac{R_q}{R_a}$ = 1.32
Roughness halfway	R_a = 1073 nm R_q = 1569 nm	$\frac{R_q}{R_a}$ = 1.46	R_a = 383 nm R_q = 489 nm	$\frac{R_q}{R_a}$ = 1.30
Roughness groove			R_a = 252 nm R_q = 341 nm	$\frac{R_q}{R_a}$ = 1.35

Figure 46 shows the primary profile at the ridge of a welding line as well as the corresponding roughness profile for λ_c = 80 µm. R_a and the R_q value were determined on the top of the ridge, on the bottom of the groove and halfway between the two. All values are displayed in table 10. The roughness was largest on the ridge and lowest in the groove, while waviness values were comparable for groove and midway with waviness being higher on the ridge. The relative discrepancy between R_a and R_q (shown in table 10) was smaller than in the case of magnesium, describing therefore a more regular roughness.
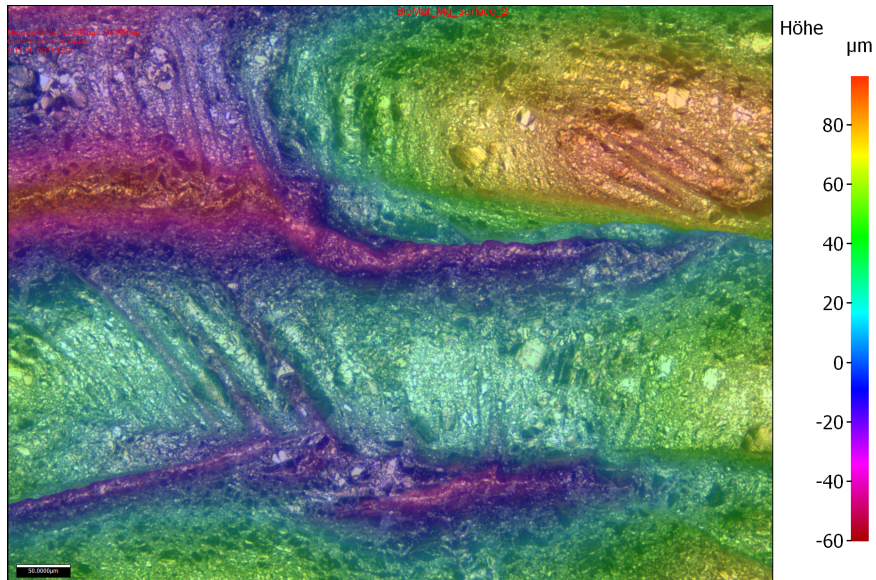
Figure 44: Magnesium surface texture: false colour height map
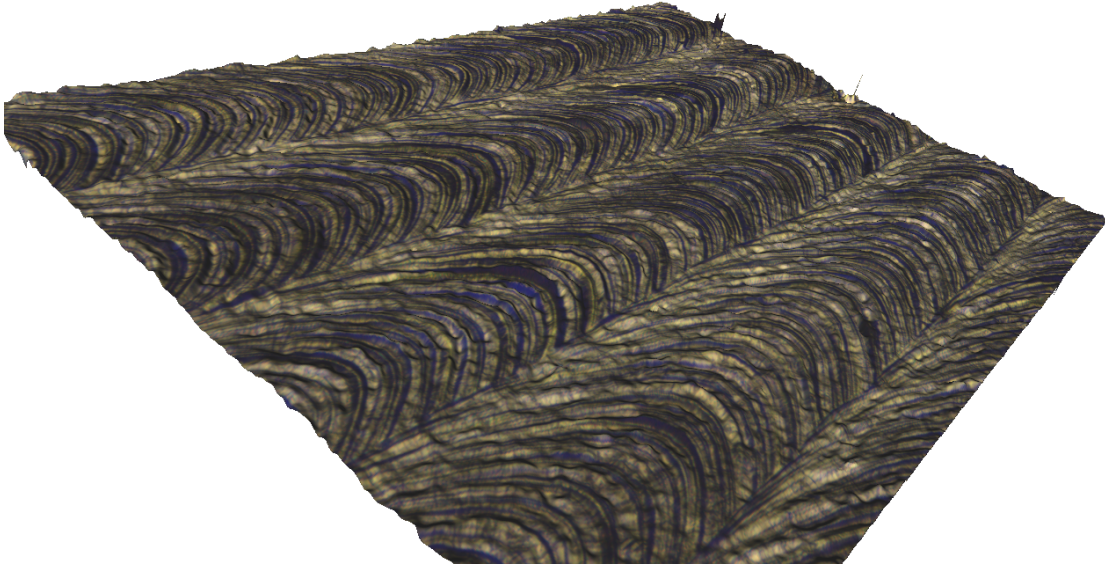
Figure 45: Alicona 3D surface picture of titanium after deep etching

There are several advantages to an increased surface roughness of titanium for biomedical application: The interlocking capacity with bone is enhanced and a beneficial effect on osteoblast adhesion has been demonstrated: Pre-osteoblastic cells were shown to proliferate on electron beam structured surfaces [60].

Finally, magnesium proved to have a beneficial effect on cell attachment and tissue growth [11]. The presence of magnesium ions (Mg^{2+}) was reported to enhance osteoblast adhesion to the substrata of biomaterials [61] which will be fundamental in the last step of magnesium degradation. As a result the interfacial shear strength between titanium and bone will increase and, consequently, improve implant stability [26, 62].

(a)

(b)
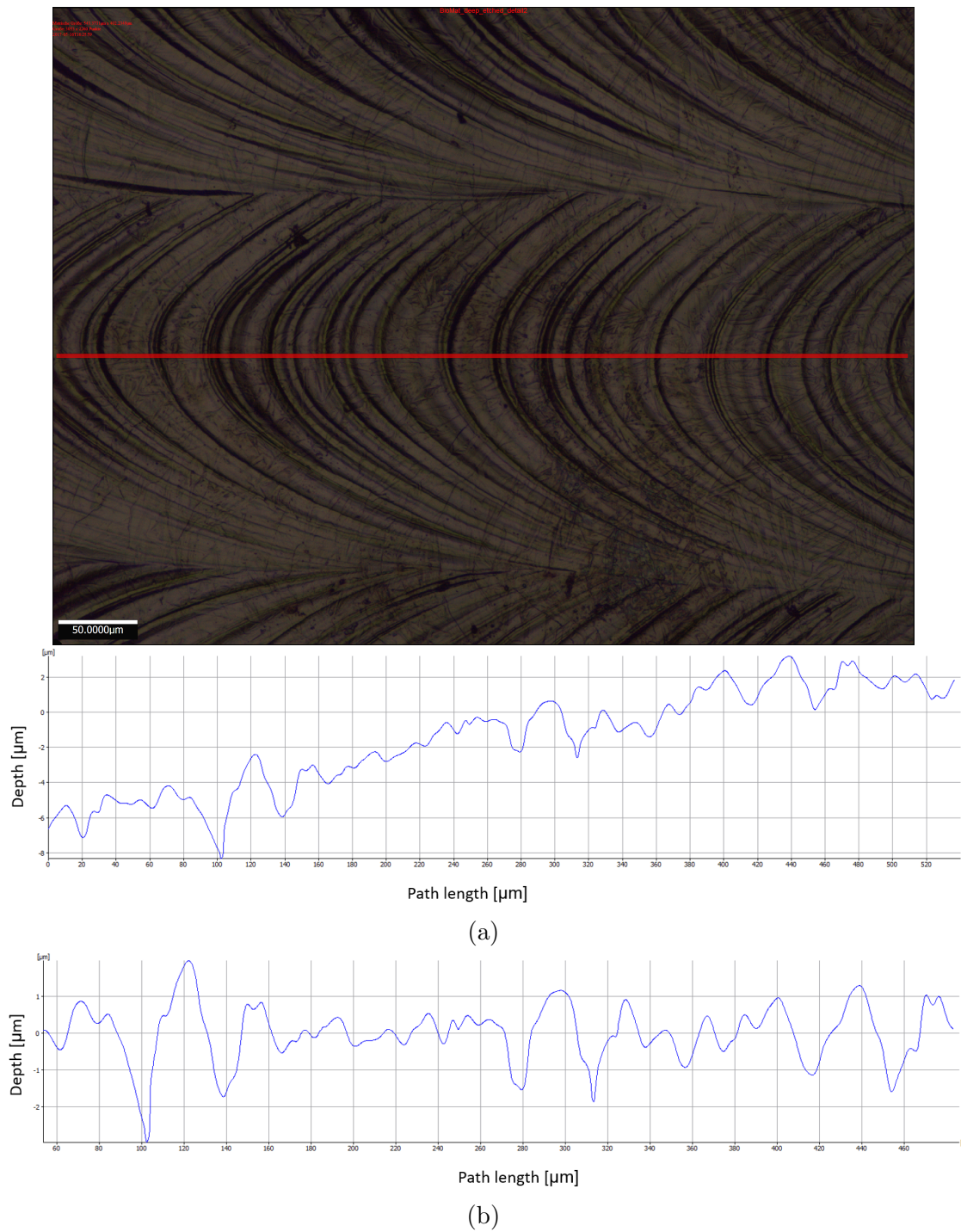
Figure 46: Titanium surface profile on the ridge of a welding line: (a) primary
profile, (b) roughness profile.

5 Summary and conclusion

In this work welding parameters were optimized and the results investigated in terms of microstructure, interface quality, surface finish, hardness and element distribution. The analysis produced the following results:

- Optimized welding parameters for different beam figures resulted in a satisfactory bonding between titanium and magnesium (I = 2 mA; line-type: frequency = 10000-20000 Hz, energy input = 4-8 J/mm^3, line spacing = 0.25 mm; random points: frequency = 2000 Hz, energy input = 20-25 J/mm^3)

- Defects in magnesium and at the interface like porosity and cracks could be avoided by a preheating and a post weld heat treatment routine performed with a current of 1 mA.

- Titanium inclusions in magnesium appeared for high energy inputs suggesting a partial melting of titanium. This could be reduced by increasing the welding speed up to (200 - 400 mm/s).

- Microstructural changes in magnesium consisted in the formation of small grains in the centre of the weld and close to the surface and interface.

- Electron beam welding of Mg2Ag resulted in a refinement of the dendritic structure and a redistribution of silver by micro and macrosegregation.

- Titanium microstructure was changed to a martensitic structure at the Mg-Ti interface with increased hardness values compared to the bulk.

- Heat treatments of the Mg2Ag alloy resulted in the formation of Mg$_4$Ag-precipitates (primarily at grain boundaries) which were larger for higher temperatures and longer ageing times.

- Alloying of pure magnesium with silver lead to an increase in hardness. Furthermore, hardness was elevated after the welding procedure. Ageing did not result in any significant hardness increase.

- Interface examination and EDX-measurements could not determine the extent of magnesium concentration in titanium and vice versa, but revealed

that the silver concentration drops to zero at the interface for the Mg2Ag alloy.

- Surface analysis of magnesium revealed welding grooves for a line-type beam figure and solidification lines around impact points as well as an increment of the surface.

- The titanium interface featured equally welding grooves and solidification lines, however with a lower roughness and a more regular surface.

5.1 Conclusion

The obtained results suggest a good interface bonding between titanium and magnesium with almost no defects neither at the interface nor in the bulk. Future application as an implant could profit from a good surface finish of magnesium and titanium alike. Osteoconductive and osteoinductive properties of magnesium may promote bone growth directly on its surface during its degradation and further support bone growth on titanium. Moreover, osseointegrative properties and favourable surface finish of titanium itself promote a stable implant-bone interface with good anchorage. Furthermore, the presence of silver with its beneficial antibacterial properties reduces the risk of infection. Finally, tribological behaviour of titanium is enhanced due to increased hardness by formation of martensite.

5.2 Outlook

Further examination of the interface with TEM are in prospect which would provide more information on the nature of bonding between magnesium and titanium. In vitro tests need to be carried out to determine degradation behaviour of magnesium in active environments as well as osteoblast proliferation behaviour on both magnesium and titanium surface which is essential for the functioning of the implant. Subsequently, the welding process can be adapted accordingly.
In order to examine the strength of the joint, bending tests should be performed to ensure that no detachment during implant forming or service life takes place.
The employment of other types of beam figures should be considered. These could

produce different, also more favourable microstructural and surface or interface characteristics.

6 Bibliography

6.1 Literature

[1] Park, Joon and Lakes, R.S.: *Biomaterials. An introduction.* New York: Springer, 2007, Third Edition.

[2] Bergmann, Carlos P. and Stumpf, Aisha: *Dental Ceramics. Microstructure, Properties and Degradation.* Berlin Heidelberg: Springer, 2013.

[3] Williams, D.F.: *The Williams Dictionary of Biomaterials.* Liverpool: University Press, 1999.

[4] Albrektsson, T.: *Osteoinduction, osteoconduction and osseointegration.* in: European Spine Journal 10, (2010), S96-S101.

[5] Ratner, Buddy D. et.al.: *Biomaterials Science. An Introduction to Materials in Medicine.* Academic Press, 2013, Third Edition.

[6] Wong, J.Y. and Bronzino, J.D.: *Biomaterials.* CRC Press, 2007.

[7] Zheng, Y.F. et.al.: *Biodegradable metals.* in: Materials Science and Engineering: R: Reports 77, (2014), 1-34.

[8] Yun, Yeoheung et.al.: *Revolutionizing biodegradable metals.* in: Materials Today 12, 10 (2009), 22-32.

[9] Kulkarni, Mukta et.al.: *Biomaterial surface modification of titanium and titanium alloys for medical applications.* in: Nanomedicine, (2014), 111-136.

[10] Y, Li et.al.: *Cytotoxicity of Titanium and Titanium Alloying Elements.* in: Journal of Dental Research 89, (2010), 493-497.

[11] Staiger, Mark P. et.al.: *Magnesium and its alloys as orthopedic biomaterials: A review.* in: Biomaterials 27, 9 (2006), 1728-1734.

[12] Brunette, D.M. et.al.: *Titanium in Medicine. Material Science, Surface Science, Engineering, Biological Responses and Medical Applications.* Berlin Heidelberg: Springer, 2001.

[13] Tosatti, Samuele G.P.: *Functionalized Titanium Surfaces for Biomedical Applications: Physic-Chemical Characterization and Biological in vitro Evaluation.* Dissertation, ETH Zürich 2003.

[14] Anil, S. et.al.: *Dental Implant Surface Enhancement and Osseointegration.* in Implant Dentistry - A Rapidly Evolving Practice, InTech, 2011.

[15] Webster, Thomas J. and Ejiofor, Jeremiah U.: *Increased osteoblast adhesion on nanophase metals: Ti, Ti6Al4V, and CoCrMo.* in: Biomaterials 25, 19 (2004), 4731-4739.

[16] Arenas, M.A. et.al.: *Corrosion behaviour of nitrogen implanted titanium in simulated body fluid.* in: British Corrosion Journal 35, 3 (2000), 232-236.

[17] Fukumoto, S. et.al.: *Surface modification of titanium by nitrogen ion implantation.* in: Materials Science and Engineering: A 263, 2 (1999), 205-209.

[18] Hsu, Shan-hui et.al.: *Characterization and biocompatibility of a titanium dental implant with a laser irradiated and dual-acid etched surface.* in: Bio-Medical Materials and Engineering 17, 1 (2007), 53-68.

[19] Yue, T.M et.al.: *Excimer laser surface treatment of Ti-6Al-4V alloy for corrosion resistance enhancement.* in: Materials Letters 52, 3 (2002), 206-212.

[20] Richard, C. et.al.: *Corrosion and wear behavior of thermally sprayed nano ceramic coatings on commercially pure Titanium and Ti-13Nb-13Zr substrates.* in: International Journal of Refractory Metals and Hard Materials 28, 1 (2010), 115-123.

[21] Lin, X. et.al.: *A Review Paper on Biomimetic Calcium Phosphate Coatings.* in: The Open Biomedical Engineering Journal 9, (2015), 56-64.

[22] Mohammed, Mohsin Talib et.al.: *Surface Modifications of Titanium Materials for developing Corrosion Behavior in Human Body Environment: A Review.* in: Procedia Materials Science 6, (2014), 1610-1618.

[23] Feyerabend, Frank et.al.: *Unphysiologically High Magnesium Concentrations Support Chondrocyte Proliferation and Redifferentiation.* in: Tissue Engineering 12, 12 (2006), 3545-3556.

[24] Witte, F. et.al.: *In vivo corrosion of four magnesium alloys and the associated bone response.* in: Biomaterials 26, 17 (2005), 3557-3563.

[25] Pichler, K. et.al.: *Cellular reactions to biodegradable magnesium alloys on human growth plate chondrocytes and osteoblasts.* in: International Orthopaedics (SICOT) 38, 4 (2014), 881-889.

[26] Castellani, Christoph et.al.: *Bone-implant interface strength and osseointegration: Biodegradable magnesium alloy versus standard titanium control.* in: Acta Biomaterialia 7, 1 (2011), 432-440.

[27] Kraus, Tanja et.al.: *Magnesium alloys for temporary implants in osteosynthesis: In vivo studies of their degradation and interaction with bone.* in: Acta Biomaterialia 8, 3 (2012), 1230-1238.

[28] Wang, Yong et.al.: *Corrosion process of pure magnesium in simulated body fluid.* in: Materials Letters 62, 14 (2008), 2181-2184.

[29] Janning, C. et.al.: *Magnesium hydroxide temporarily enhancing osteoblast activity and decreasing the osteoclast number in peri-implant bone remodelling.* in: Acta Biomaterialia 6, 5 (2010), 1861-1868.

[30] Prabhakar, A.R. et.al.: *Comparative evaluation of pH and antibacterial effect of various calcium hydroxide combinations on E. faecalis and its effect on root strength: An in vitro study.* in: Contemporary Clinical Dentistry 3, 1 (2012), 42-47.

[31] Tie, D. et.al.: *Antibacterial biodegradable Mg-Ag alloys.* in: European Cells and Materials 25, (2013), 284-298.

[32] Atiyeh, Bishara S. et.al.: *Effect of silver on burn wound infection control and healing: Review of the literature.* in: Burns 33, 2 (2007), 139-148.

[33] Drynda, Andreas et.al.: *Rare earth metals used in biodegradable magnesium-based stents do not interfere with proliferation of smooth muscle cells but do induce the upregulation of inflammatory genes.* in: Journal of Biomedical Materials Research 91A, 2 (2009), 360-369.

[34] Zhang, Shaoxiang et.al.: *Research on an Mg-Zn alloy as a degradable biomaterial.* in: Acta Biomaterialia 6, 2 (2010), 626-640.

[35] Kirkland, N.T. et.al.: *A survey of bio-corrosion rates of magnesium alloys.* in: Corrosion Science 52, 2 (2010), 287-291.

[36] Palmer, Ronald J. et.al.: *Cytotoxicity of the rare earth metals cerium, lanthanum, and neodymium in vitro: Comparisons with cadmium in a pulmonary macrophage primary culture system.* in: Environmental Research 43, (1987), 142-156.

[37] Bosetti, M. et.al.: *Silver coated materials for external fixation devices: in vitro biocompatibility and genotoxicity.* in: Biomaterials 23, 3 (2002), 887-892.

[38] Hardes, Jendrik et.al.: *The Influence of Elementary Silver Versus Titanium on Osteoblasts Behaviour In Vitro Using Human Osteosarcoma Cell Lines.* in: Sarcoma 2007, (2007).

[39] *Phase diagrams.* Retrieved from `http://www.himikatus.ru/` [April 2017].

[40] Hoffmann, Ilona: *Magnesium-Titanium Alloys for Biomedical Applications.* Dissertation, University of Kentucky 2014.

[41] Zheng, J.G. et.al.: *Microstructure of vapour quenched Ti-29 wt.%Mg alloy solid solution.* in: Journal of Materials Science 32, 12 (1997), 3089-3099.

[42] Asano, Kohta et.al.: *Synthesis process of Mg-Ti BCC alloys by means of ball milling.* in: Journal of Alloys and Compounds 486, 1 (2009), 115-123.

[43] Song, Guang-Ling et.al.: *The corrosion and passivity of sputtered Mg-Ti alloys.* in: Corrosion Science 104, (2016), 36-46.

[44] Garcés, G. et.al.: *Texture of magnesium alloy films growth by physical vapour deposition (PVD).* in: Journal of Alloys and Compounds 309, (2000), 229-238.

[45] Garcés, G. et.al.: *Precipitation hardening of Mg-12% Ti (wt.%) synthetised by physical vapour deposition.* in:Materials Science and Engineering: C 56, (2015), 241-250.

[46] Liu, Yong et.al.: *Powder metallurgical low-modulus Ti-Mg alloys for biomedical applications.* in: Scripta Materialia 45, (2001), 1001-1007.

[47] Volker, Adam et.al.: *Electron beam welding. The fundamentals of a fascinating technology.* pro-beam AG & Co. KGaA, 2011.

[48] Schubert, G.: *Electron beam welding - Process, Applications and Equipment.* PTR-Precision Technologies Inc.

[49] Oktay, Gizem et.al.: *Magnesium Films Deposited on Titanium via Arc PVD Method.* in: Materials Science Forum 546-549, (2007), 519-522.

[50] Ren, Daxin et.al.: *Ultrasonic spot welding of magnesium alloy to titanium alloy.* in: Scripta Materialia 126, (2017), 58-62.

[51] Matweb, LLC. *Material property data.*
Retrieved from `http://www.matweb.com` [May 2017].

[52] Aerospace Specification Metals, INC. *Titanium Grade 2.*
Retrieved from `http://asm.matweb.com/search/SpecificMaterial.asp?bassnum=MTU020` [May 2017].

[53] OLYMPUS CORPORATION. *Roughness Terminology.*
Retrieved from `http://www.olympus-ims.com/en/knowledge/metrology/roughness` [May 2017].

[54] Kammerer, Catrin: *Magnesium Taschenbuch.* Aluminium-Zentrale Düsseldorf, Düsseldorf, 2000, 1. Auflage.

[55] Gu, Dongdong et.al.: *"Densification behavior, microstructure evolution, and wear performance of selective laser melting processed commercially pure titanium.* in: Acta Materialia 60, 9 (2012), 3849-3860.

[56] Zheng, Yufeng: *Magnesium Alloys as Degradable Biomaterials.* CRC Press, 2015.

[57] Wang, Mark L. et.al.: *Direct and indirect induction of apoptosis in human mesenchymal stem cells in response to titanium particles.* in: Journal of Orthopaedic Research 21, 4 (2003), 697-707.

[58] Wang, Mark L. et.al.: *Scaling of titanium implants entrains inflammation-induced osteolysis.* in: Scientific Reports 7, (2017).

[59] ImageJ. *Image Processing and Analysis in Java.* Retrieved from `https://imagej.nih.gov/ij/` [June 2017].

[60] Ramskogler, Claudia et.al.: *Innovative surface modification of Ti6Al4V alloy by electron beam technique for biomedical application.* in: Materials Science and Engineering: C 78, (2017), 105-113.

[61] Zreiqat, H. et.al.: *Mechanisms of magnesium-stimulated adhesion of osteoblastic cells to commonly used orthopaedic implants.* in: Journal of biomedical materials research 62, 2 (2002), 175-184.

[62] Revell, P.A. et.al.: *The Effect of Magnesium Ions on Bone Bonding to Hydroxyapatite Coating on Titanium Alloy Implants.* in: Key Engineering Materials 254-256, (2004), 447-450.

7 Appendix

7.1 List of Figures

7.2 List of Tables

7.3 MATLAB Code

```matlab
% Program with the correct number of supporting points of EBW
% x / y machine max = 65535;
% the program may occupy only 40000 points (storage limit)
%%%%%% ENTER %%%%%%%%%%%%%%%%%%%%%%%%%%%%%%%%%%%%%%%%%%
    SWX = 10;                        %sample dimension X direction [mm] (diameter)
    line_density = 50;               %density along one line [pts/mm]
    spacing = 0.25;                  %spacing between lines [mm]
    geometry = 'random';             %lines,grid,random
    nr_points_random = 10000;        %how many random points to create

    max_machinepoints=65535;         %number of the maximum coordinate. the
    calculation is rounded to an even number
%%%%%%%%%%%%%%%%%%%%%%%%%%%%%%%%%%%%%%%%%%%%%%%%%%%%%%%

mm_to_machine=floor(max_machinepoints/SWX); %Increment in x direction (convert mm
    to coordinate data)
a=[];
b=[];

if isequal(geometry,'lines')
    for y=0:round(spacing*mm_to_machine):max_machinepoints
        for x=0:floor(max_machinepoints/line_density/SWX):max_machinepoints
        a=[a x];
        b=[b y];
        end
    end

    xaus=a'; %transpose (from rows to columns)
    yaus=b';

    final_matrix=[xaus yaus]; %final matrix to be stored as file
    max_points = size(final_matrix,1); %number of points

    %%%%%% file writing %%%%%%%%%%%%%%%%%%%%%%%%%%%%%%%%%%%%
    dlmwrite(sprintf('%dptsDen_%dpts_SWX%3.1f_lineSpacing%3.4f_%s.b01',
    line_density,max_points,SWX,spacing,geometry),final_matrix,'delimiter', '\t','
    newline', 'pc');
                    %the data is saved in a b01 file
                    %the attrib 'delimeter' is set to TAB, while
                    %'newline'is set to pc=carriage return/line feed

elseif isequal(geometry,'grid')
    for y=0:round(spacing*mm_to_machine):max_machinepoints
        for x=0:floor(max_machinepoints/line_density/SWX):max_machinepoints
        a=[a x];
        b=[b y];
        end
```

```matlab
      end

    xaus=a'; %transpose (from rows to columns)
    yaus=b';

    %%%%% create grid %%%%%%%%%%%%%%%%%%%%%%%%%%%%%%%%%%%%%

    final_matrix = [[xaus;yaus],[yaus;xaus]];
    max_points = size(final_matrix,1);

    %%%%% file writing %%%%%%%%%%%%%%%%%%%%%%%%%%%%%%%%%%%%%

    dlmwrite(sprintf('%dptsDen_%dpts_SWX%3.1f_lineSpacing%3.4f_%s.b01',
    line_density,max_points,SWX,spacing,geometry),final_matrix,'delimiter', '\t','
    newline', 'pc');

    %%%%% random ordered elements in matrix %%%%%%%%%%%%%%%%%
    %final_matrix = final_matrix(randperm(size(final_matrix,1)),:);
    %random = 'random';

elseif isequal(geometry,'random')

    %%%%% random points in square %%%%%%%%%%%%%%%%%%%%%%%%%%%
    final_matrix = [randi(max_machinepoints,nr_points_random,1),randi(
    max_machinepoints,nr_points_random,1)];
    max_points = size(final_matrix,1);

    dlmwrite(sprintf('%dpts_SWX%3.1f_%s.b01',max_points,SWX,geometry),final_matrix
    ,'delimiter', '\t','newline', 'pc');

end

%%%%% plot data %%%%%%%%%%%%%%%%%%%%%%%%%%%%%%%%%%%%%%%%%%%
figure
plot(final_matrix(:,1),final_matrix(:,2),'.')
title(sprintf('%s data visualization',geometry))
xlabel('x')
ylabel('y')
axis([0 max_machinepoints 0 max_machinepoints])
axis square
%axis equal
```